

Changes of Early Summer Precipitation in the Korean Peninsula and Nearby Regions Based on RCP Simulations

JA-YOUNG HONG AND JOONG-BAE AHN

Division of Earth Environmental System, Pusan National University, Busan, South Korea

(Manuscript received 16 July 2014, in final form 13 January 2015)

ABSTRACT

In this study, the projected regional precipitation changes over northeast Asia (NEA) during early summer [May–July (MJJ)] for the late twenty-first century (2071–2100) were investigated using a high-resolution regional climate model (WRF3.4) based on the representative concentration pathways (RCPs) induced by the global circulation model (HadGEM2-AO). The increased horizontal resolution of the regional model with a 12.5-km horizontal resolution enabled it to reproduce the terrain-following features reasonably well compared to low-resolution reanalysis and HadGEM2-AO model data. The results of a regionally downscaled historical (1981–2010) experiment (D_Historical) demonstrated the model's ability to capture the spatial and temporal variations of rainband migrating meridionally during MJJ over NEA. According to the regional model projection, intensive precipitation will increase and the rainband will affect the Korean Peninsula approximately 10 days earlier than in the D_Historical cases in both RCP4.5 and RCP8.5 (2071–2100). The precipitation will also increase in most of the domain, particularly in the southern Korean Peninsula and Kyushu, Japan. These increases in precipitation are attributed to increases in the northward moist transport coming from the lower latitudes and moist static instability in the lower atmosphere. According to this study, the convective precipitation contributes mainly to the increase in total precipitation. On the other hand, the large-scale nonconvective precipitation related to the stationary front will not change significantly but even tends to decrease approximately from the middle of July. The extreme precipitation intensity is also projected to increase by at least 22% (38%) in RCP4.5 (RCP8.5).

1. Introduction

The summer precipitation in East Asia (EA) can be divided into the precipitation accompanied by the rainbands related to the stationary front called baiu in Japan, changma in the Korean Peninsula, and mei-yu in China (BCM) and the precipitation that occurs locally due to convective instability during the period that EA is dominated by the North Pacific high. In particular, the lengthy rainbands appearing across EA during early summer are one of the major characteristics of the EA summer monsoon (EASM) and appear markedly in June and July (Fig. 1). These rainbands, which are related to more than 40% of the summer rainfall in EA,

account for a major part of the precipitation in this region (Oh et al. 1997; Ding and Chan 2005). EASM is one of the major components of the Asian summer monsoon (ASM) system (Tao and Chen 1987; Wang and Chen 2012; Ding et al. 2014). EASM, which is related to seasonal changes in large-scale atmospheric circulations in the EA region (Qian and Zhu 2002; Ding and Chan 2005), consists of tropical, subtropical, and midlatitude weather systems. Owing to the distinctive topography and orography (Liu et al. 2008; Hsu et al. 2014), EASM has complicated characteristics that are different from those of the South Asian summer monsoon (so-called Indian summer monsoon), which is in the tropical monsoon system (Liu et al. 1994; Wang et al. 2008; Zhou et al. 2009).

Previous studies attributed the weakened EASM to global warming (e.g., Hu et al. 2003; Wu et al. 2006; Wang et al. 2012; Zhu et al. 2012), weakening of the correlation between ENSO and EASM (e.g., Hu 1997; Wang 2002; Wu and Wang 2002), increases in black carbon aerosols (e.g., Xu 2001; Menon et al. 2002; Ramanathan et al. 2005), upper-troposphere cooling (e.g., Yu et al. 2004; Yu and Zhou 2007), decreases in snow cover and snow depth

Denotes Open Access content.

Corresponding author address: Joong-Bae Ahn, Department of Atmospheric Sciences, Pusan National University, 2, Busandaehak-ro 63beon-gil, Geumjeong-gu, Busan 609-735, South Korea.
E-mail: jbahn@pusan.ac.kr

DOI: 10.1175/JCLI-D-14-00504.1

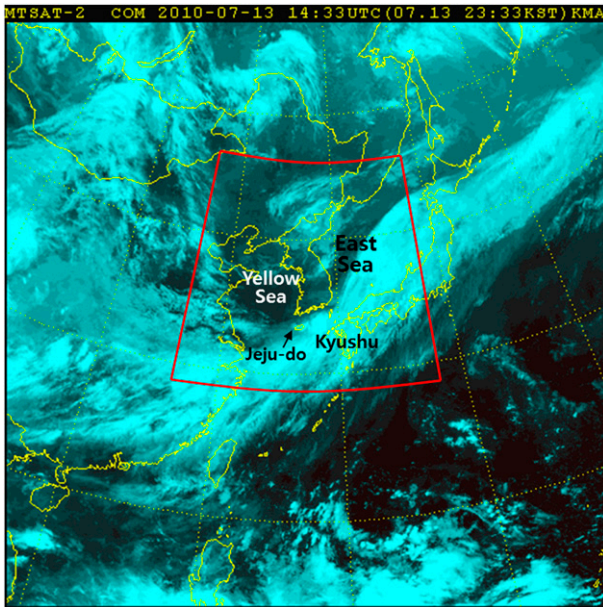


FIG. 1. Synthetic image at 1433 UTC 13 Jul 2010 observed by *Multifunctional Transport Satellite-2* (MTSAT-2). This shows a view of the clouds that appear frequently in the MJJ season. The cloud band stretching from southern China through the southern sea to Japan was made by the BCM front, and it brought heavy rain in China, the Korean Peninsula, and Japan during this period while moving repeatedly northward and southward. The region enclosed by the red lines is the domain examined in this study.

over the Tibetan Plateau (e.g., Qian et al. 2003; Liu and Wang 2011), and the climate regime shift in the 1970s (e.g., Wang 2001; Ding et al. 2008). Nevertheless, the true cause remains unclear, and the changing reactions of EASM to global warming, in particular, are still controversial.

Several studies have examined changes in the intensity and impact of EASM due to future climate change. Using the Special Report on Emission Scenarios (SRES) multi-model ensemble (MME) of the Intergovernmental Panel on Climate Change (IPCC), Kripalani et al. (2007) estimated that precipitation in the Korean Peninsula, China, and Japan regions would increase significantly by approximately 10% because of intensification of the projected North Pacific subtropical high. Using the IPCC SRES A1B scenario, Sun and Ding (2010) also argued that summer precipitation in EA would be enhanced by the intensification of monsoon circulation and increases in water vapor transported northward into East China. Using the 25-yr future prediction data of a 20-km mesh global atmospheric model produced based on A1B, Kusunoki and Mizuta (2008) suggested that summer precipitation in the Yangtze River valley would increase. Meanwhile, in an A1B scenario, Tanaka et al. (2005) and Ueda et al. (2006) estimated that, although summer precipitation would increase, the ASM circulation would be weakened by

approximately 15%. In an IPCC A1B scenario, Li et al. (2010) suggested that the long-term trend of EASM variations would be neither strengthening nor weakening.

Recently, the IPCC has adopted new scenarios of potential future anthropogenic climate change, representative concentration pathways (RCPs) (Meinshausen et al. 2011) based on phase 5 of the Coupled Model Intercomparison Project (CMIP5). Using the CMIP5 models, Chen and Sun (2013) suggested that, in the RCP4.5 scenario, EA summer precipitation and its intensity might increase in the near (2016–35) and long-term (2080–99) future. Using the RCP4.5 and RCP8.5 scenarios and the Regional Climate Model, version 4, Oh et al. (2014) proposed that the EA summer precipitation in the future (2031–50) would increase by 5% compared to that of the present (1986–2005) and that heavy rainfall ($>50 \text{ mm day}^{-1}$) would also increase. Gao et al. (2013) also simulated future climate changes over China with a horizontal resolution of 50 km based on RCP4.5 and RCP8.5. They projected a general increase in annual-mean precipitation over northwestern China in the future (2080–99). However, since previous RCP-related studies used low-resolution model data or showed summer-mean results, detailed climate change analyses with spatially and temporally high-resolution model data are necessary.

In this study, dynamically downscaled simulations produced by RCP4.5- and RCP8.5-based scenarios were used to examine the changes in the BCM front and resulting changes in precipitation in northeast Asia (NEA) centered on the Korean Peninsula. To this end, the downscaled historical simulation was also compared with observations to analyze the reproducibility of the dynamic model to estimate the temporal and spatial variations of this front and its associated precipitation.

2. Data and experimental method

Dynamical downscaling was conducted using the Weather Research and Forecasting (WRF), version 3.4. The initial and boundary conditions for WRF were the outputs of the Hadley Centre Global Environmental Model, version 2–Atmosphere and Ocean (HadGEM2-AO) based on historical, RCP4.5, and RCP8.5 scenarios. The HadGEM2-AO simulations were conducted by the National Institute of Meteorological Research/Korea Meteorological Administration (NIMR/KMA). The individual downscaled experiments were called D_Historical, D_RCP4.5, and D_RCP8.5, respectively. Time-varying CO_2 (Meinshausen et al. 2011) based on RCP4.5 and RCP8.5 was applied to D_RCPs for future projection. The NIMR/KMA is jointly participating in the CMIP5 long-term experiment with the Met Office Hadley Centre using HadGEM2-AO (Baek et al. 2013). HadGEM2-AO

showed good performance in simulating the temperature and precipitation over NEA, particularly the Korean Peninsula, in terms of annual cycle, precipitation pattern and timing of rainy season (Lee et al. 2009, 2010). The horizontal resolution of the atmospheric model of HadGEM2-AO was $1.875^\circ \times 1.250^\circ$. Please refer to Collins et al. (2011) for detailed specifications of HadGEM2-AO.

The analysis domain of WRF is a region centered on the Korean Peninsula and including part of Japan and China ($29^\circ\text{--}46^\circ\text{N}$, $117^\circ\text{--}138^\circ\text{E}$) (red line domain in Fig. 1). A map projection is Lambert conformal and the geographical resolution is 5 min. The horizontal resolution is 12.5 km and the center of model domain is located at 37.5°N , 127.5°E . The vertical grids are composed of 28 terrain-following hydrostatic levels stretching from the surface to 50 hPa (top of the model).

Regarding the physics used in WRF integration, the WRF single-moment three-class scheme (Hong et al. 2004) was chosen for the microphysics. The National Center for Atmospheric Research (NCAR) Community Atmospheric Model scheme (Collins et al. 2002) was used for the longwave and shortwave radiation, and the Monin–Obukhov similarity theory (Jiménez et al. 2012) was applied to the surface layers. In addition, the Noah Land Surface Model (Chen and Dudhia 2001) and the Yonsei University scheme (Hong et al. 2006) were used for the land surfaces and planetary boundary layers, respectively. The cumulus convective parameterization scheme is important for the simulation of precipitation (Zheng et al. 1995; Sénési et al. 1996; Giorgi and Shields 1999). In this study, the Kain–Fritsch scheme (Kain 2004) was used for cumulus convective parameterization. This scheme is known to simulate the timing of the maximum rainfall occurrence reasonably well and showed the capability to reproduce the spatial and temporal distributions of precipitation over EA (Lee and Park 2002; Yu et al. 2011). The options for diffusion on coordinate surfaces and horizontal eddy coefficient were the second-order diffusion and Smagorinsky first-order closure, respectively. The integration time step was 60 s, and the radiation and cumulus physics calls were set to 30 and 5 min, respectively. The variables were stored on an hourly basis.

WRF considers leap years, whereas HadGEM2-AO sets 1 yr as 360 days. Therefore, the 360 days of data were interpolated into the 365 or 366 days of data using the NCAR Command Language and the Grid Analysis and Display System. The interpolated data were converted to intermediate files of WRF using the Formula Translator. The period of D_Historical was 32 yr from 1979 to 2010 and the first 2 yr were regarded as a model spinup period and not used in the analysis. Although the

integration period of D_RCP4.5 and D_RCP8.5 was 2019–2100 in this study, only the last 30 yr of data (2071–2100) were used for the analysis. The analysis variable was the daily (both convective and nonconvective) precipitation from May to July (MJJ). Without removing the bias, the performance of WRF in the D_Historical experiment in this analysis was evaluated. However, the systematic model bias in the projected analyses was regarded to have been removed since the difference was obtained by subtracting D_RCPs from D_Historical (Ahn et al. 2012). Fractional changes in precipitation [e.g., the ratios of (D_RCPs – D_Historical) to D_Historical] are illustrated for each D_RCP.

The observed precipitation data used to compare the D_Historical simulation results are the Tropical Rainfall Measuring Mission (TRMM) 3B42 version 7 daily merged rainfall (Huffman et al. 2007). The horizontal resolution of TRMM was 0.25° and its data period was 1998–2014. The description of CMIP5 models available for the period 1981–2010 used for MME is illustrated in Table 1. MME was obtained using the simple ensemble-mean method for the first members of the individual model. In addition, monthly precipitation of 60 stations of South Korea from the KMA was used for the period 1981–2010.

To analyze the spatial evolution of precipitation over time, the cyclostationary empirical orthogonal function (CSEOF) (Kim and North 1997) was obtained. In this method, space–time precipitation data $P(r, t)$ are written as a linear superposition of the CSEOFs,

$$P(r, t) = \sum_n P_n(r, t) PC_n(t), \quad (1)$$

where $P_n(r, t)$ and $PC_n(t)$ are the CSEOF spatial patterns and corresponding principal component (PC) time series, respectively, and n , r , and t denote the mode number, space, and time, respectively. The CSEOF spatial patterns are time dependent and periodic: that is,

$$P_n(r, t) = P_n(r, t + d), \quad (2)$$

where d is called the nested period. The CSEOF spatial patterns represent temporally evolving physical processes, whereas the PC time series represent the amplitude modulation of the physical processes on longer time scales (Kim and Roh 2010). The CSEOF analysis was conducted on the 30-yr record of every 10-day average from 31 May to 29 July. Thus, the nested period was set to be 6.

3. Analysis of simulation

a. Evaluation of HadGEM2-AO and WRF3.4

In this study, the BCM front was replaced with changma for any discussion confined to the Korean

TABLE 1. CMIP5 model used for MME in this study.

Modeling group	Model name
Commonwealth Scientific and Industrial Research Organization (CSIRO) and Bureau of Meteorology (BOM), Australia	ACCESS1.0
Beijing Climate Center, China Meteorological Administration	BCC_CSM1.1
College of Global Change and Earth System Science, Beijing Normal University	BNU-ESM
Canadian Centre for Climate Modeling and Analysis	CanESM2
Community Earth System Model Contributors	CESM1 (CAM5)
Centro Euro-Mediterraneo per I Cambiamenti Climatici	CMCC-CM
Centre National de Recherches Météorologiques/Centre Européen de Recherche et Formation Avancée en Calcul Scientifique	CNRM-CM5
Commonwealth Scientific and Industrial Research Organization in collaboration with Queensland Climate Change Centre of Excellence	CSIRO Mk3.6.0
LASG, Institute of Atmospheric Physics, Chinese Academy of Sciences and CESS, Tsinghua University	FGOALS-g2
First Institute of Oceanography, State Oceanic Administration (SOA), China	FIO-ESM
National Oceanic and Atmospheric Administration/Geophysical Fluid Dynamics Laboratory	GFDL CM3 GFDL-ESM2G GFDL-ESM2M
National Aeronautics and Space Administration Goddard Institute for Space Studies	GISS-E2-H GISS-E2-R
National Institute of Meteorological Research/Korea Meteorological Administration	HadGEM2-AO
Met Office Hadley Centre (additional HadGEM2-ES realizations contributed by Instituto Nacional de Pesquisas Espaciais)	HadGEM2-CC HadGEM2-ES
Institute for Numerical Mathematics	INM-CM4
Institut Pierre-Simon Laplace	IPSL-CM5A-LR IPSL-CM5A-MR IPSL-CM5B-LR
Japan Agency for Marine-Earth Science and Technology, Atmosphere and Ocean Research Institute (University of Tokyo) and National Institute for Environmental Studies	MIROC-ESM MIROC-ESM-CHEM
Atmosphere and Ocean Research Institute (University of Tokyo), National Institute for Environmental Studies, and Japan Agency for Marine-Earth Science and Technology	MIROC5
Max-Planck-Institut für Meteorologie (Max Planck Institute for Meteorology)	MPI-ESM-LR MPI-ESM-MR
Meteorological Research Institute	MRI-CGCM3
Norwegian Climate Centre	NorESM1-M NorESM1-ME

Peninsula. Figure 2 shows a comparison of the MJJ-mean precipitation of CMIP5 MME, HadGEM2-AO, and D_Historical with that of TRMM. According to TRMM (Fig. 2a), the maximum precipitation was centered on southeastern Japan but ranged widely from the east to the west across the Korean Peninsula and China. The second peak of precipitation appeared in the southeastern region of China. CMIP5 MME simulated weak precipitation associated with the BCM front and an overall level of precipitation in this region that was smaller than that of TRMM (Fig. 2b). The precipitation simulated by HadGEM2-AO (Fig. 2c) was stronger (weaker) than TRMM in the southeastern marine region of Japan (in the southeastern region of China). The center of precipitation was located slightly southward compared to TRMM. Although the precipitation in the 35°–40°N region in HadGEM2-AO was simulated slightly smaller than TRMM, the precipitation pattern toward the Korean Peninsula was simulated as being

similar to TRMM. Because D_Historical is high-resolution data, the characteristic distributions of the regional precipitation following terrain was simulated in more detail than TRMM and other models (Fig. 2d). The maximum precipitation area was located in the southern coast region of Japan and in the ocean to the south of Japan in the form of bifurcation, and the second peak was simulated on the southeast of China. Although D_Historical simulated slightly larger precipitation than HadGEM2-AO, its precipitation in the Korean Peninsula was more similar to the observations. The precipitation of D_Historical in South Korea was compared with the meteorological station observation in Fig. 2e. D_Historical simulated well the regional precipitation distribution that is not depicted by CMIP5 MME and HadGEM2-AO. Therefore, D_Historical simulated appropriately the amount and distribution of precipitation during MJJ in the region centered on the Korean Peninsula.

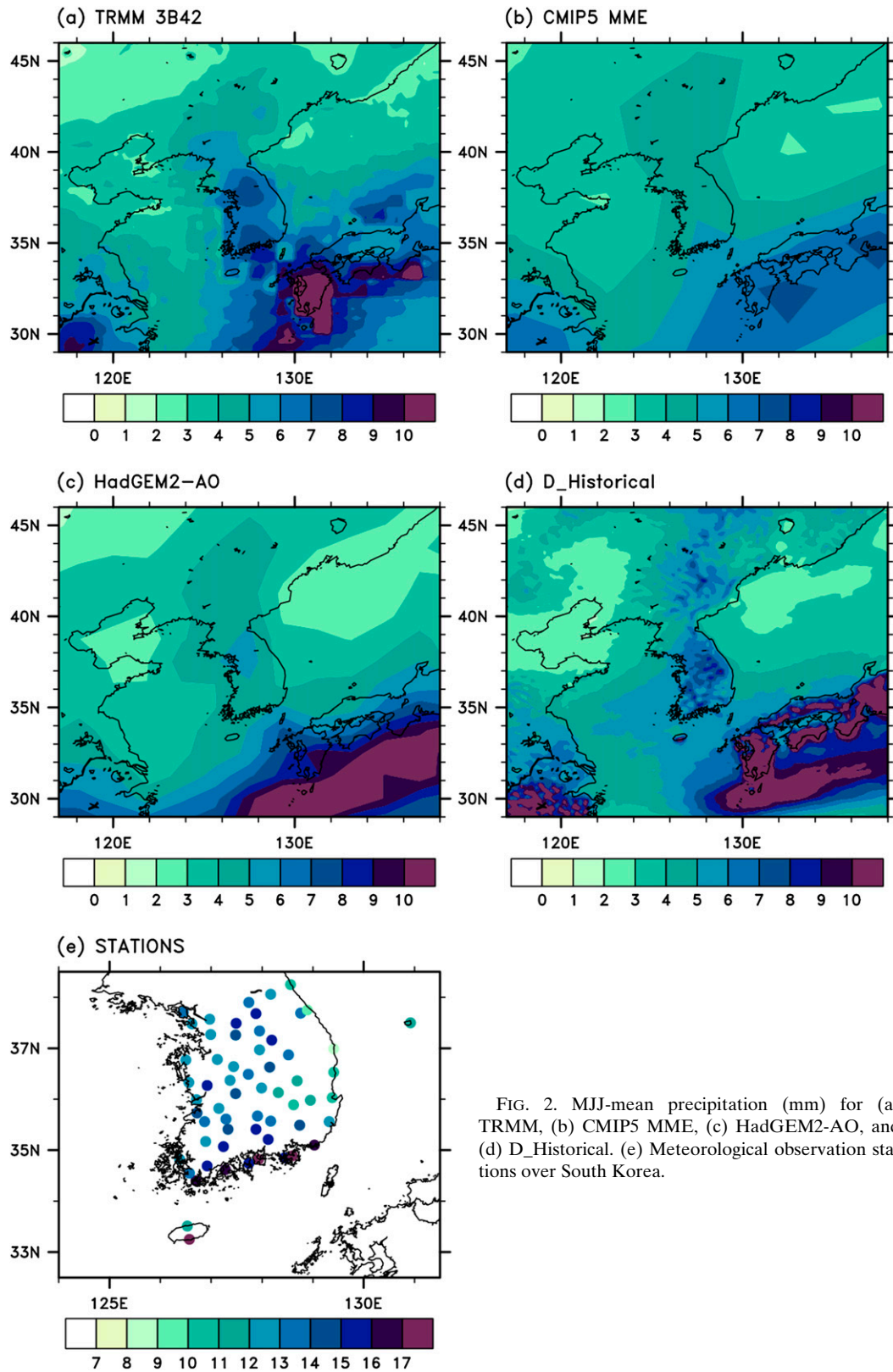


FIG. 2. MJJ-mean precipitation (mm) for (a) TRMM, (b) CMIP5 MME, (c) HadGEM2-AO, and (d) D_Historical. (e) Meteorological observation stations over South Korea.

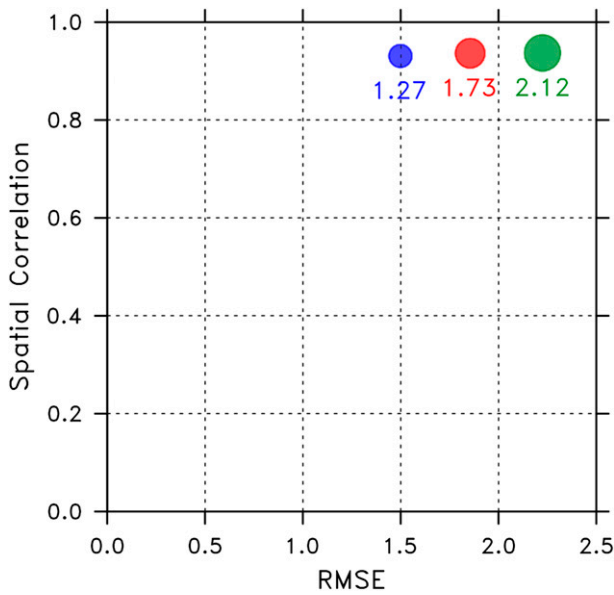


FIG. 3. Scatterplot of MJJ-mean precipitation from CMIP5 MME (green), HadGEM2-AO (blue), and D_Historical (red) relative to TRMM over northeast Asia (29° – 46° N, 117° – 138° E). The numbers in the figure and the size of the circles indicate the bias.

Figure 3 displays the root-mean-square errors (RMSEs), spatial correlations, and bias of MJJ precipitation from CMIP5 MME (green), HadGEM2-AO (blue), and D_Historical (red) with respect to TRMM over the domain. The RMSE and bias of D_Historical were larger (smaller) than those of HadGEM2-AO (CMIP5 MME). The larger RMSE and bias in D_Historical seems to be due to the error inherited from HadGEM2-AO. The spatial correlation coefficients of the models were in the similar range of 0.93–0.94, which indicated that D_Historical showed a similar level of performance in simulating the MJJ precipitation patterns compared to CMIP5 MME and HadGEM2-AO.

Figure 4 presents the time series of MJJ-mean domain-averaged precipitation changes simulated by HadGEM2-AO and WRF3.4. The two models show similar temporal evolutions under the same scenarios. The correlation coefficients between HadGEM2-AO and WRF3.4 precipitations for each RCP result were statistically significant at the 1% significance level.

b. BCM front

The time–latitude plots of the 124° – 132° E zonal-mean precipitation of TRMM and D_Historical are shown in Fig. 5. The precipitation is the pentad data obtained by averaging every 5 days. As shown in TRMM, the precipitation related to the changma front that begins in late May at 30° N moves systematically northward

thereafter. This northward movement of the maximum precipitation is due to the movement of the changma-related stationary front because the North Pacific High expands northward during this period. The precipitation of at least 10 mm day^{-1} moves northward to the north of 40° N by the middle of July. The D_Historical precipitation begins in the middle of May, earlier than TRMM, and moves northward thereafter until July. The speed and latitude of the northward movements of the rainbands in the Korean Peninsula of D_Historical were similar to those of TRMM. On the other hand, D_Historical estimated that the precipitation north of 34° N would be weaker than TRMM.

Figure 6 shows the first CSEOF modes of the TRMM and D_Historical precipitations averaged for every 10 days from 31 May to 29 July. The first CSEOF modes that account for 22% and 21% of the total variances of TRMM and D_Historical, respectively, well depicted the development and northward movements of the rainbands related to the changma front in this region. According to TRMM, positive precipitation appears in the southern ocean of Japan around early June (31 May–9 June). The Korean Peninsula begins to be affected by the positive precipitation from approximately early July (30 June–9 July). This positive precipitation moves northward and appears strongly and markedly between 32° and 42° N around the middle of July (10–19 July) and its center is located in the central part of the Korean Peninsula. The positive precipitation moves to the northern part of the Korean Peninsula or farther northward around late July (20–29 July) and becomes weaker thereafter. This northward migration of positive precipitation occurring in the Korean Peninsula from the middle of June to late July is related to the changma front and is an important characteristic of early summer precipitation in this region (Lee and Seo 2013; Moteki and Manda 2013).

In the analyzed domain, the changes and development of positive precipitation in D_Historical were quite similar to those in TRMM (Fig. 6b). The positive precipitation develops in the southern ocean of Japan around early June (31 May–9 June) and strong positive precipitation is shown in this region until late June (20–29 June). The positive precipitation moves northward to the southern sea of the Korean Peninsula around early July (30 June–9 July), similarly to TRMM. Most regions to the north of 34° N are affected by this rainband in the middle of July (10–19 July). In late July (20–29 July), this positive precipitation moves to the region of 117° – 130° E to the north of 34° N, including the Korean Peninsula. Owing to the difference in spatial resolution between D_Historical and TRMM, the rainband in D_Historical is narrower than that in TRMM with a lower resolution.

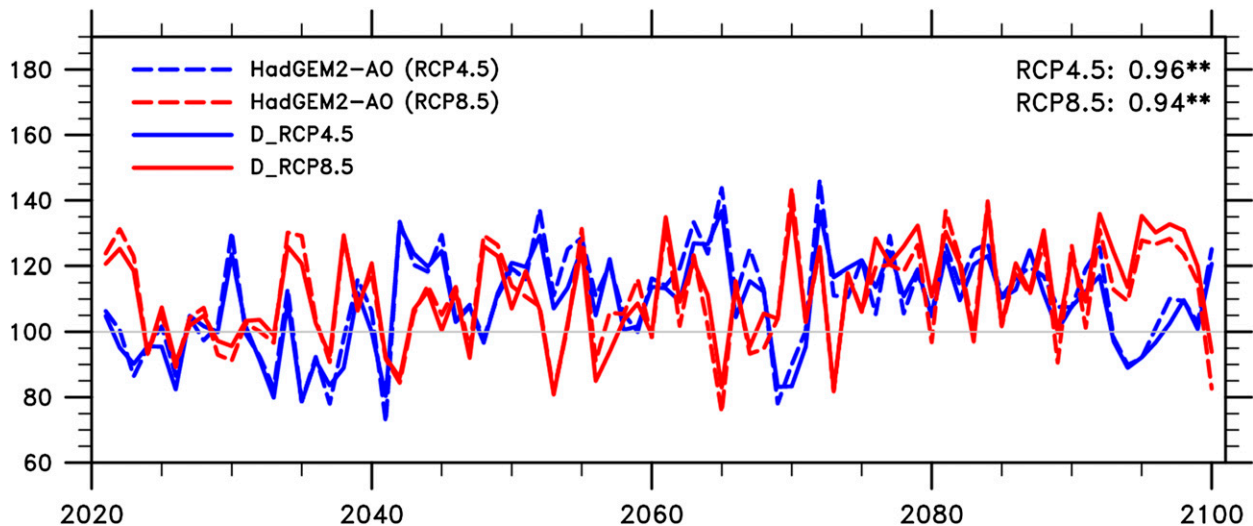


FIG. 4. Regional-mean changes in MJJ-mean precipitation (%) over northeast Asia (29° – 46° N, 117° – 138° E) simulated by HadGEM2-AO (dashed lines) and WRF (solid lines) in RCP4.5 (blue) and RCP8.5 (red) relative to historical (1981–2010). The numbers in the top right of the figure are correlation coefficients between HadGEM2-AO and WRF. The two asterisks indicate statistical significance at the level of 1%.

Temporally, the rainband in D_Historical develops approximately 10 days later than that in TRMM and lasts for approximately 10 days. Through the analysis mentioned above, although the rainband in D_Historical moves northward slightly later, its spatial distribution, northward movement speed, and duration period are similar to those of TRMM. Therefore, the major pattern of the BCM front-related precipitation of D_Historical is similar to that of TRMM. This suggests that down-scaled WRF simulation based on the HadGEM2-AO data can well depict the characteristic pattern of precipitation in this region. Therefore, the major changes in the pattern of precipitation by D_RCP4.5 and D_RCP8.5 are also expected to be reliable.

4. Comparative analysis of D_RCPs and D_Historical

a. Changes in the rainband

Figure 7 shows the first mode of CSEOF for precipitation during the MJJ period of D_RCP4.5 and D_RCP8.5. The differences between the two D_RCPs and D_Historical were calculated by removing the average of D_Historical from the individual RCPs. The fractional variances of the first mode of D_RCP4.5 and D_RCP8.5 were 21% and 24%, respectively, which were similar to those of D_Historical. In the case of D_RCP4.5, although positive differences appear in the southern ocean of Japan in early June (31 May–9 June) identically to D_Historical, the sizes of the difference

were smaller than those of D_Historical (Fig. 7a). Thereafter, the positive differences developed gradually to affect the entire region to the south of 35° N, including the southern part of the Korean Peninsula in late June (20–29 June). D_RCP4.5 exhibits the largest positive difference in the Korean Peninsula in early July (30 June–9 July), approximately 10 days earlier compared to that of D_Historical and its intensity is higher than that of D_Historical. This difference weakens and moves northward thereafter to affect the region to the north of 35° N in late July (20–29 July). That is, in the case of D_RCP4.5, although the changma fronts develop in the southern ocean of Japan at a similar time to those in D_Historical, the peak period of changma in the Korean Peninsula is expected to develop approximately 10 days earlier and stronger than that in D_Historical and move northward to the northern region of the Korean Peninsula approximately 10 days earlier than that in D_Historical.

In the case of D_RCP8.5, the positive differences are located to the north of those in D_Historical in early June (31 May–9 June) and the magnitudes were smaller than those in D_Historical but identical to D_RCP4.5 (Fig. 7b). Strong positive differences develop lengthily from the east to the west in the region south of 34° N, including Jeju-Do of South Korea and Japan in the middle of June (10–19 June). The center of these positive differences is located to the northwest of that of D_Historical or D_RCP4.5 in the same period and is stronger. The positive differences start to affect the entire Korean Peninsula in late June (20–29 June) and

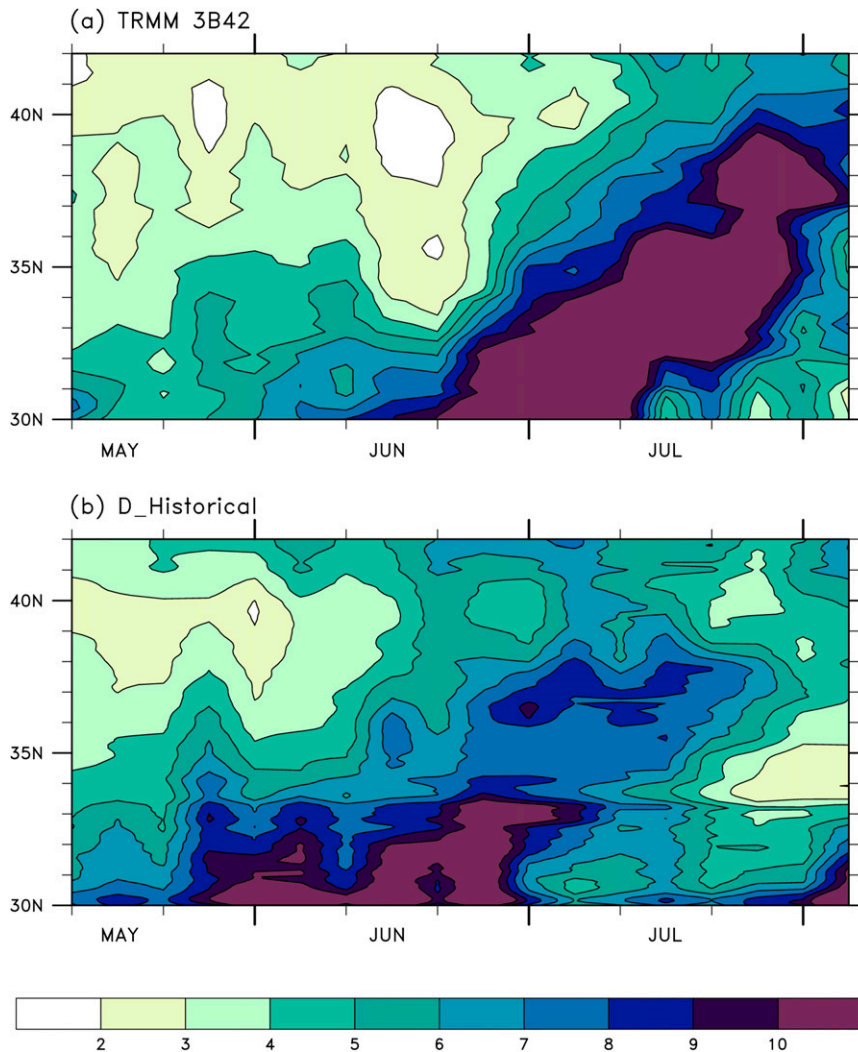


FIG. 5. Hovmöller plot of MJJ precipitation (mm day^{-1}) over the Korean Peninsula (124° – 132°E) for (a) TRMM and (b) D_Historical.

reach a peak in early July (30 June–9 July). During this period, the intensity of the positive differences in the Korean Peninsula was shown to be stronger than those of D_Historical and D_RCP4.5. These positive differences weakly affect the entire Korean Peninsula until the middle of July (10–19 July) and move to the northern region of the Korean Peninsula in late July (20–29 July). Therefore, in the case of D_RCP8.5, as with D_RCP4.5, the changma fronts develop approximately 10 days earlier than D_Historical and changma lasts until late July in the Korean Peninsula, but the rainbands in late July in the Korean Peninsula are expected to be clearly weaker than those in D_Historical. In addition, during the CSEOF analysis period, the precipitation intensity in the Korean Peninsula by D_RCP8.5 is expected to be higher than that in the case of D_Historical or D_RCP4.5.

To examine the changes in precipitation according to the RCP scenarios, the differences in the evolution of 124° – 132°E zonally averaged pentad-mean precipitation between D_RCPs and D_Historical are shown as a latitude–time plot (Fig. 8). The red dots indicate the statistically significant regions at the 5% significance level of the t test. The differences between D_RCPs and D_Historical are shown as shading and the D_Historical means are drawn as contours. The time series below and to the right of the latitude–time plot are the area-averaged precipitation change over the southern part of South Korea (33° – 36°N , 124° – 132°E) and the mean precipitation percentage change during the period from 21 May to 9 July, respectively.

In the case of D_RCP4.5, the precipitation in the 30° – 38°N region (south of the central part of the Korean

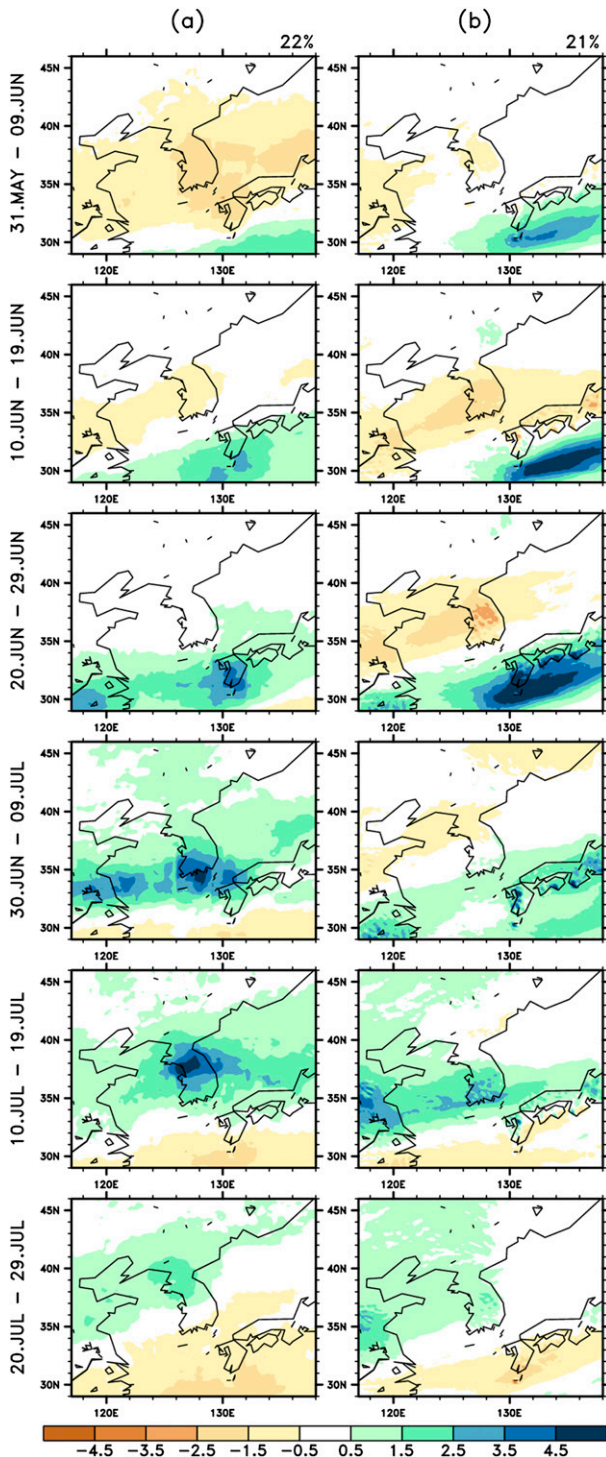


FIG. 6. First mode of CSEOF for precipitation from (a) TRMM and (b) D_Historical. The period of data is (top to bottom) 31 May–20 Jul. The digits represent fractional variances explained by each CSEOF first mode.

Peninsula) was projected to be slightly smaller than that in D_Historical in late May and early June (Fig. 8a). From the middle of June, when the rainbands in D_Historical develop and move northward (Fig. 6b), the precipitation in D_RCP4.5 was much larger than that in D_Historical in the 30° – 33° N region (the southern seas of the Korean Peninsula and Kyushu of Japan); in early July, the precipitation was much larger in the entire region south of 36° N (south of the southern region of the Korean Peninsula). On the other hand, the precipitation in the 34° – 40° N region (the Korean Peninsula) in the middle of June was smaller than that in D_Historical. This means that the latitudinal variations of precipitation become large even within the Korean Peninsula. The precipitation in the 33° – 37° N region (central and southern parts of the Korean Peninsula) in the middle of July and thereafter is smaller than or similar to that in D_Historical. That is, the mean precipitation in the southern region of the Korean Peninsula in D_RCP4.5 becomes larger than that in D_Historical from late June to early July and becomes smaller than that in D_Historical in the middle of July (lower time series of Fig. 8a). The mean precipitation during this period in D_RCP4.5 is larger than that in D_Historical in the 31° – 37° N region (right-side time series of Fig. 8a).

The precipitation in D_RCP8.5 (Fig. 8b) is similar to or slightly larger than that in D_Historical in most regions until late May. The precipitation in the region south of 33° N in late May and early June is slightly larger than that in D_Historical, which is in contrast to that in D_RCP4.5. From mid to late June, the precipitation in the region south of 34° N (south of the southern part of the Korean Peninsula) is much larger than that in D_Historical, and the precipitation in the 34° – 37° N region (central and southern parts of the Korean Peninsula) is similar to or slightly smaller than that in D_Historical. This means that the rainbands in D_RCP8.5 develop stronger than those in D_Historical in the southern seas of the Korean Peninsula and Japan. Therefore, the precipitation in these regions increases, whereas the central and southern regions of the Korean Peninsula are dryer than those in D_Historical. In early July, the precipitation is much larger than that in D_Historical in the entire region south of 40° N (up to the northern part of the Korean Peninsula). Hence, as with D_RCP4.5, the latitudinal variations of precipitation are larger. In the middle of July, precipitation becomes larger than that in D_Historical in the 38° – 44° N region (northern part of the Korean Peninsula) and the precipitation in the region south of 38° N becomes similar to or slightly smaller than that in D_Historical. In late July, the rainband moves farther northward and the precipitation increases slightly in the region north of 40° N and

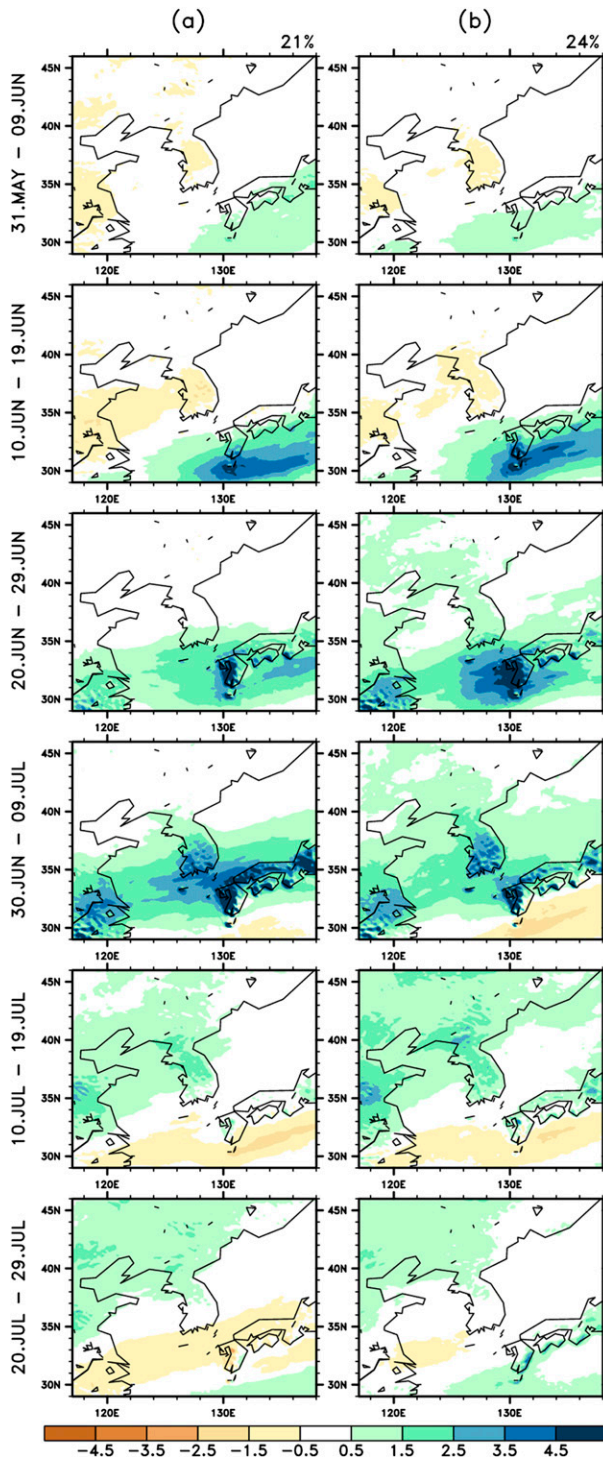


FIG. 7. As in Fig. 6, but for (a) D_RCP4.5 and (b) D_RCP8.5 (2071–2100).

decreases slightly in the 35°–39°N region (central and southern parts of the Korean Peninsula). In late July and early August, precipitation increases considerably in the region south of 34°N and is larger than that in D_RCP4.5.

This increase in precipitation is different from the increase in the changma period and will be discussed again in section 4c. The mean precipitation in the southern region of the Korean Peninsula in D_RCP8.5 is larger than that in D_Historical from late June to early July, and the magnitude of the increase is similar to that in D_RCP4.5 (lower time series of Fig. 8b). Thereafter, it decreases slightly to become smaller than that in D_Historical in the middle of July but the magnitude of the decrease is smaller than that in D_RCP4.5. The MJJ average precipitation in D_RCP8.5 increases in 31°–40°N, and this increase appears over a wide region for a longer period than that of D_RCP4.5 (right time series of Fig. 8b).

These results of D_RCPs mean that the rainbands in D_RCPs develop approximately 10 days earlier and stronger than those in D_Historical to move northward approximately 10 days earlier than those in D_Historical and that precipitation also increases greatly during the changma period. In addition, these results also imply that because of the early northward movement of rainbands, although precipitation may increase in the north of the Korean Peninsula and even in Manchuria (the region north of 42°N), the changma in the Korean Peninsula may terminate approximately 10 days earlier or may be weakened in the late changma period (mid to late July).

b. Synoptic changes in D_RCPs during MJJ

Figures 9 and 10 display the climatological difference fields between D_RCPs and D_Historical for 30 yr of MJJ, respectively. The red dots indicate statistically significant regions at the 5% significance level of the *t* test. In the case of D_RCP4.5, the surface temperatures increase by at least 2°C in the entire domain and increase relatively more in the northwest inland region above 43°N and in the East Sea (Fig. 9a). The precipitation increases in almost the entire region in the domain except for a region in the Yellow Sea. In particular, it increases greatly by at least 30% in the western coastal region of Kyushu, Japan and the southern region of the Japanese Islands (Fig. 9b). The 850-hPa geopotential height increases in the entire region due to the increase in thickness caused by the overall temperature increases in the lower atmosphere due to global warming (Fig. 9c). The increases are clear in the northeastern part of China, which is the northern inland area. Owing to the differential regional increases of the 850-hPa geopotential height, anomalous low-level moisture flows enter from the East China Sea into the northeastern region of China and Japan (Fig. 9d). The decrease in the 200-hPa zonal winds in the inland region centered on 39°N (Fig. 9e) is related to the weakened meridional geopotential gradient contrast due to the differential warming between over the high latitude inland region

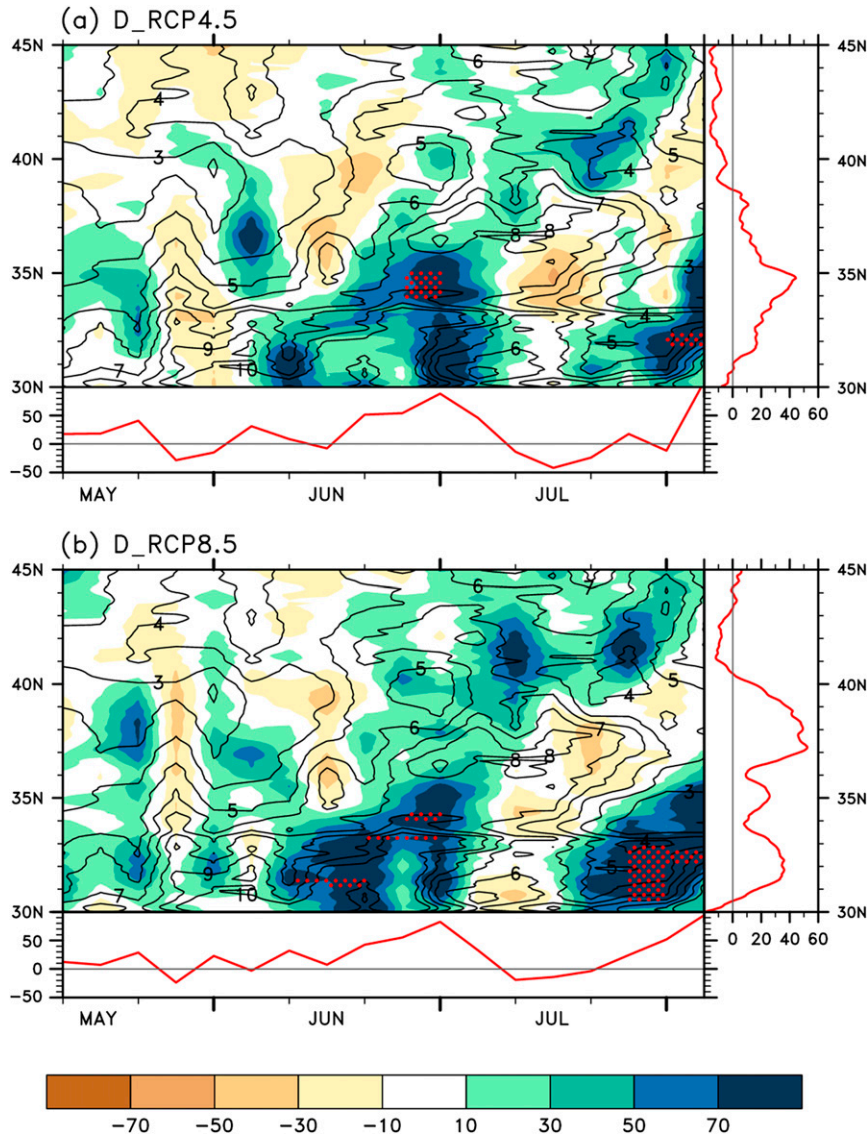


FIG. 8. Hovmöller plot of changes (shading) in 30-yr-mean precipitation for (a) D_RCP4.5 and (b) D_RCP8.5 over the Korean Peninsula (124° – 132° E). The contours are the D_Historical mean for 1981–2010. The time series under and to the right of the Hovmöller plots are area-averaged precipitation over the south region of the Korean Peninsula (33° – 36° N, 124° – 132° E) and MJJ-mean (21 May–9 Jul) percentage changes for D_RCPs over 124° – 132° E, respectively. The units of percentage changes and D_Historical-mean precipitation are percent and millimeters per day, respectively. The red dotted stippling indicates statistical significance at the 5% level of the t test.

and over the southern marine region. Figure 9f shows the distribution of the velocity potential (χ) defined as $\mathbf{V} = -\nabla \cdot \chi$. The weakening of the 200-hPa subtropical zonal winds in Fig. 9e appears to be attributable directly to the decreased zonal angular momentum because the Hadley circulation was weakened due to the increase in anomalous winds toward the equator (Held and Soden 2006; Vecchi and Soden 2007; Gastineau et al. 2008, 2009; Levine and Schneider 2011).

In the case of D_RCP8.5, the increases of surface temperature are more pronounced compared to D_RCP4.5 (Fig. 10a). Precipitation also clearly increases in most inland regions in the domain with larger areas and greater magnitudes of increase compared to D_RCP4.5 (Fig. 10b). In particular, when compared to Fig. 2d, in D_RCP8.5, the rainband related to precipitation increases greatly. The 850-hPa geopotential height increases by at least 10 gpm compared to that in

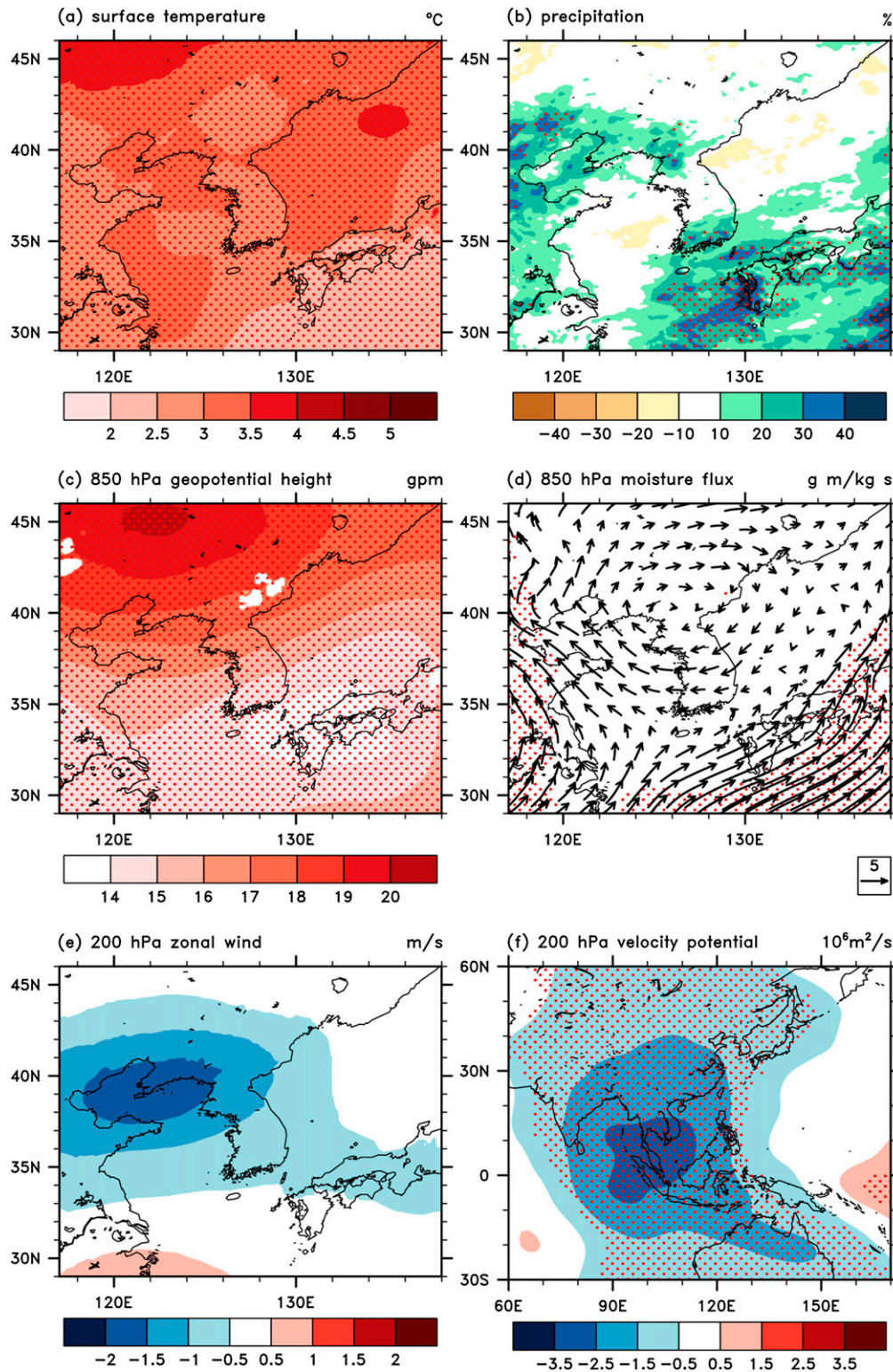


FIG. 9. Changes in MJJ-mean (a) surface temperature, (b) precipitation, (c) 850-hPa geopotential height, (d) 850-hPa moisture flux, and (e) 200-hPa zonal wind for D_RCP4.5. (f) The 200-hPa velocity potential for HadGEM2-AO. The red dotted stippling indicates statistical significance at the 5% level of the t test.

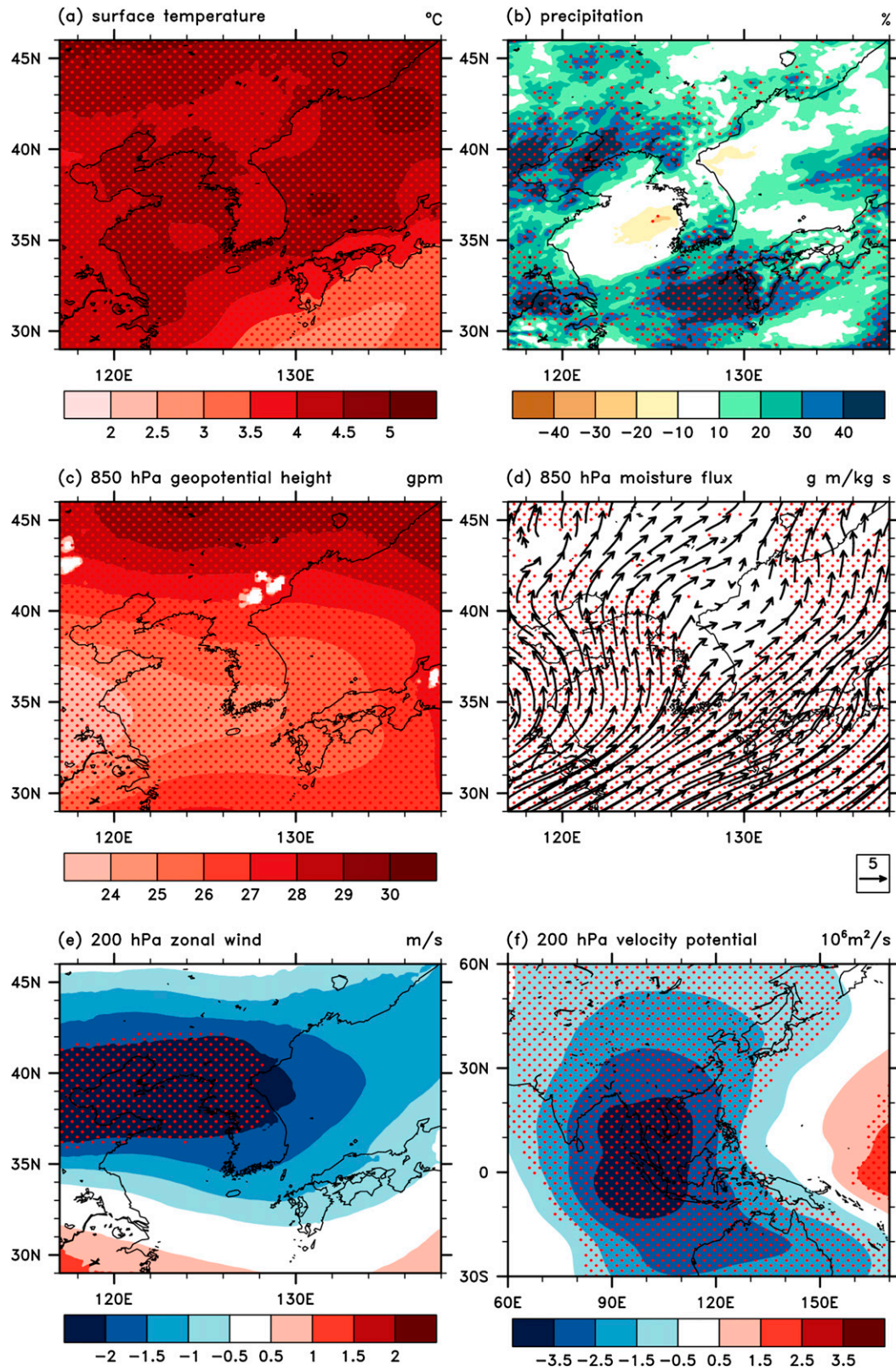


FIG. 10. As in Fig. 9, but for D_RCP8.5.

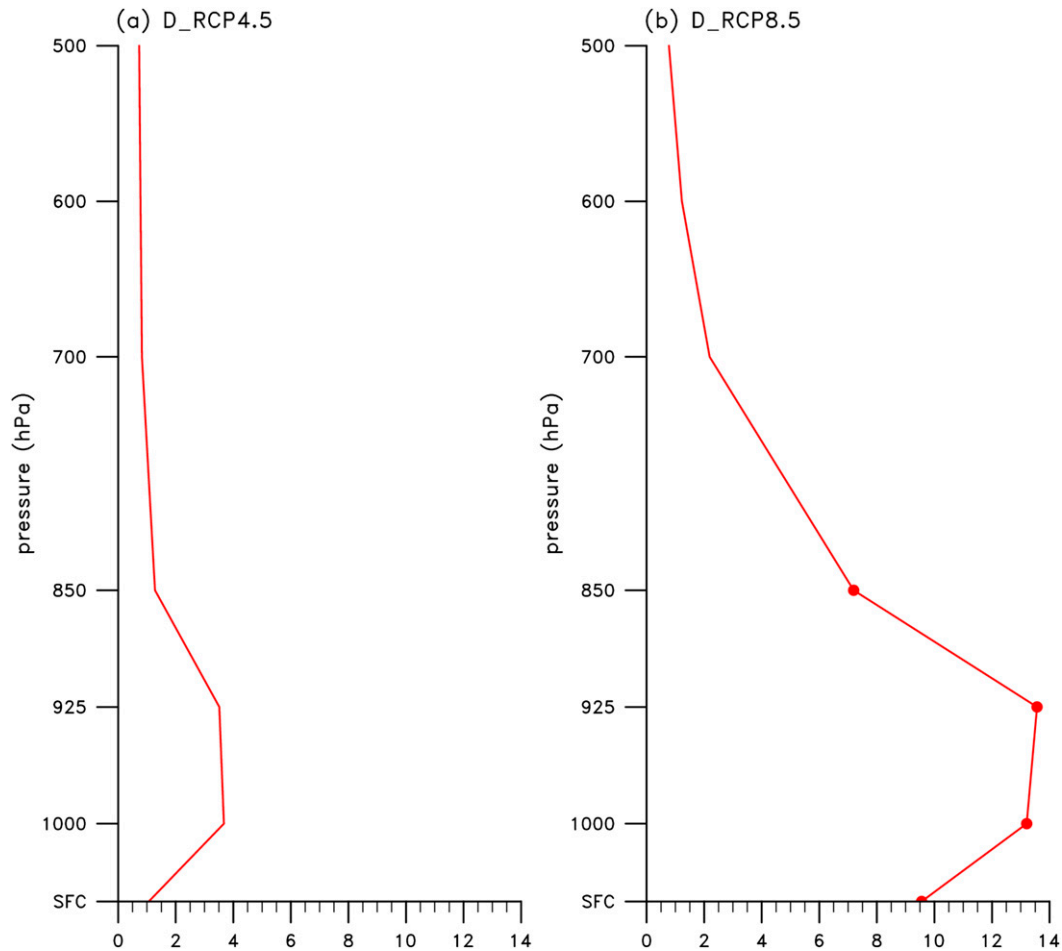


FIG. 11. Changes in meridional moisture transport over the south region of the Korean Peninsula and Kyushu in Japan (33° – 36° N, 124° – 132° E) for (a) D_RCP4.5 and (b) D_RCP8.5. Unit is $\text{g m kg}^{-1} \text{s}^{-1}$. The red dots indicate statistical significance at the 5% level of the t test.

D_RCP4.5. Particularly, it increases considerably in the northern region (Fig. 10c). In addition, as with D_RCP4.5, due to the differential increases in geopotential, anomalous northeastward flows appear that traverse from the northwestern Pacific through the Yellow Sea, the northeastern region of China, and the East Sea to the southern region of Russia (Fig. 10d). The difference in the 850-hPa moisture flux is larger than that in the case of D_RCP4.5. The 200-hPa zonal winds clearly indicate decreasing patterns in most regions and a decrease by at least 2 m s^{-1} in 35° – 45° N (Fig. 10e). As with the case of D_RCP4.5, the 200-hPa zonal winds are weakened because of the conservation of angular momentum according to the weakening of the poleward upper winds due to decreases in vertical motions in the rising branch of Hadley circulations centered on the Maritime Continent (Fig. 10f). The changes in the 200-hPa velocity potential are more prominent than those in the case of D_RCP4.5.

Figure 11 shows the vertical profiles of the changes in the meridional moisture transport (qV) averaged for the southern region of the Korean Peninsula and Kyushu in Japan (33° – 36° N, 124° – 132° E), in which the increases in precipitation have been clearly projected. In the case of D_RCP4.5, meridional moisture transport increases from the surface to 500 hPa. In particular, the increases are clear at levels below 850 hPa (Fig. 11a). Although the changes in D_RCP8.5 show similar results to those in D_RCP4.5, the magnitudes of the changes are larger than those in D_RCP4.5, and these changes are statistically significant at the 5% significance level of the t test (Fig. 11b). In particular, meridional moisture transport in D_RCP8.5 is reinforced greatly at levels not higher than 700 hPa. Therefore, increases in northward moisture transport at low levels appear more likely to contribute to the increase in precipitation in the region.

The Korean Peninsula has a stronger precipitation increase but weaker temperature increase as compared

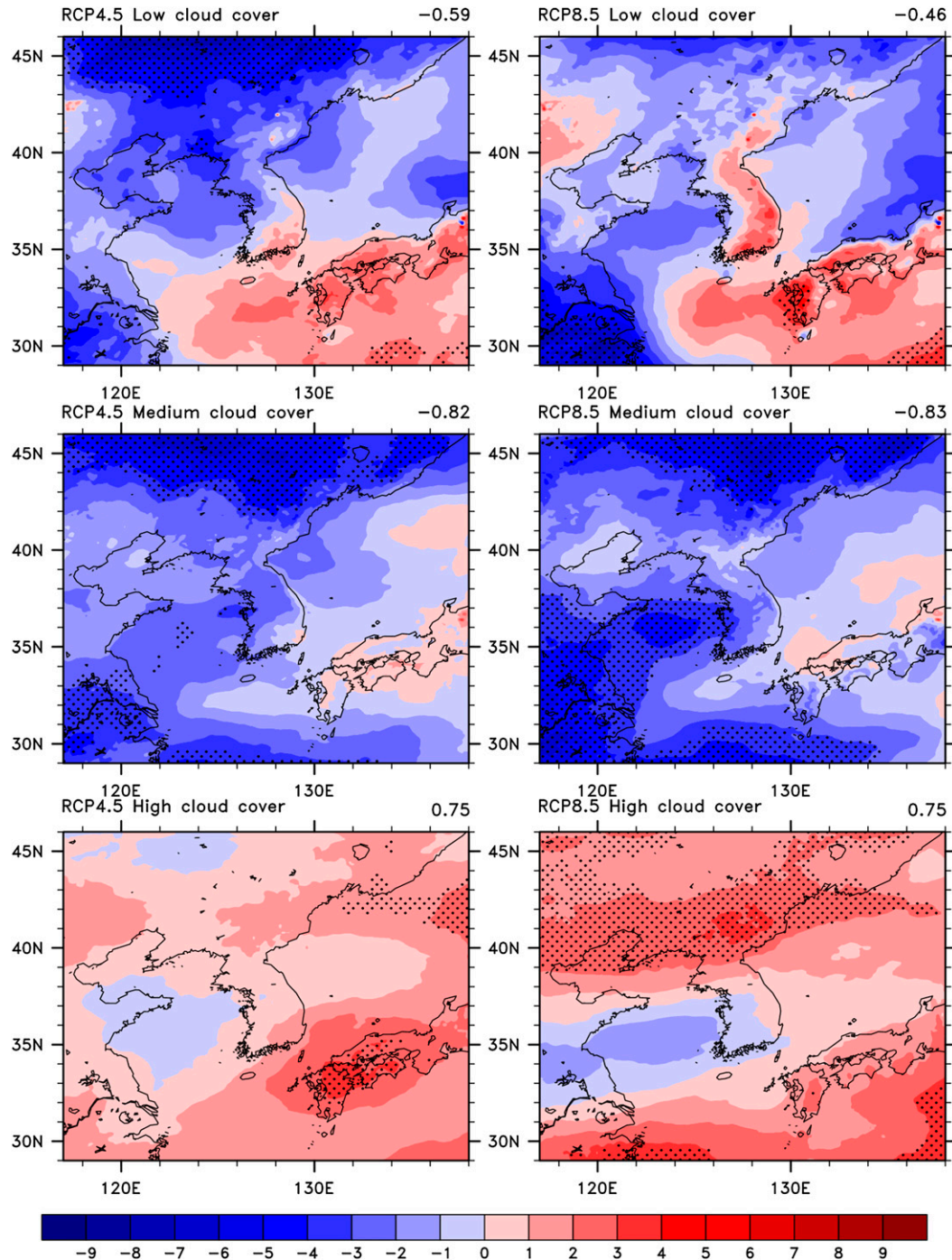


FIG. 12. Changes in (top to bottom) low, medium, and high cloud fractions. Units are $10^{-2}\%$. The numeral above the right side of each panel is the pattern correlation coefficient between cloud fraction and surface temperature. The black stippling indicates statistical significance at the 5% level of the t test.

to the surrounding oceans. This might be due to the cooling effect according to the increase of cloudiness by reduced shortwave radiation over the increased precipitation area. The comparatively greater increase in shallow clouds over the peninsula may contribute to the

weaker warming as compared to the neighboring oceans. In fact, the surface temperature has high pattern correlation with the medium and high cloud covers, as shown in Fig. 12. It is also attributed to the evaporative cooling effect in the increased precipitation area. Ahn

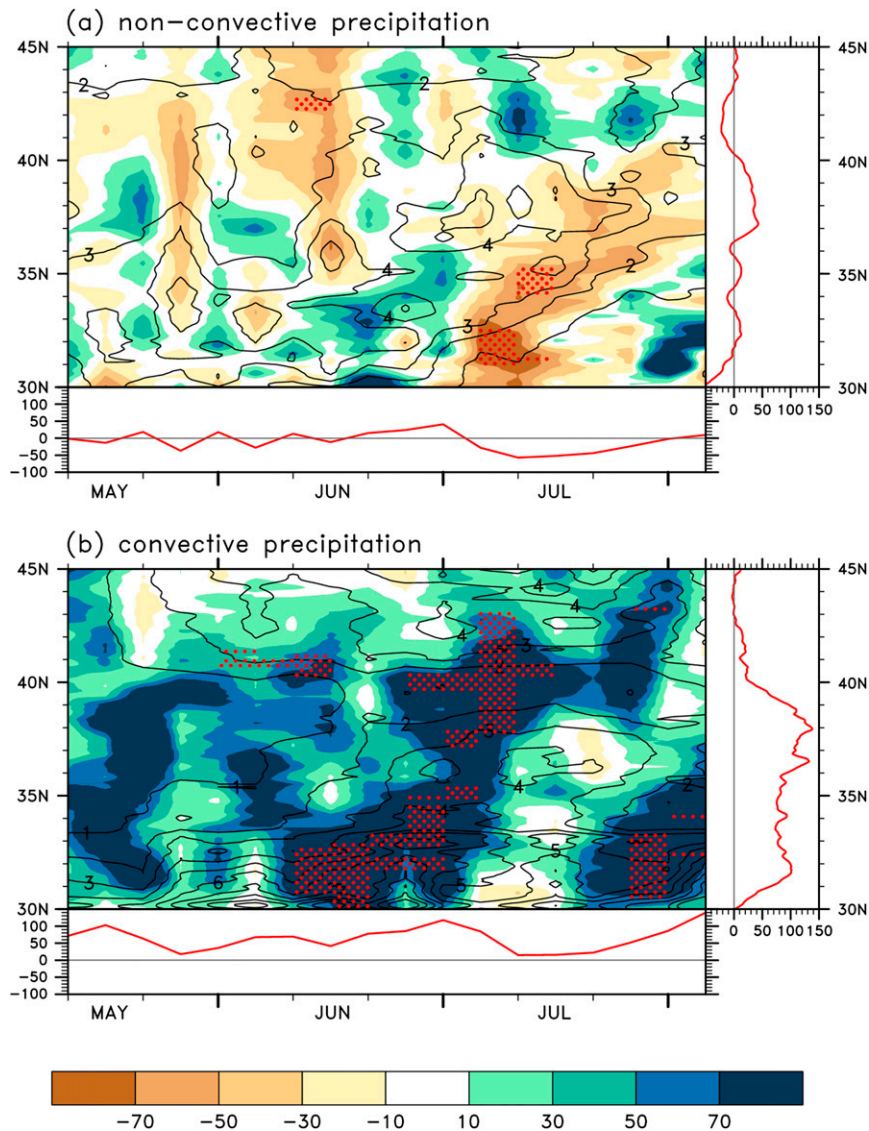


FIG. 13. As in Fig. 8, but for (a) nonconvective precipitation and (b) convective precipitation for D_RCP8.5.

et al. (1997) argued that the summer (nonsummer) precipitation is negatively (positively) correlated with temperature in the Korean Peninsula. In this region, the precipitations of summer and the other seasons are mostly due to the convective activities and the large-scale extratropical synoptic system activities, respectively. They also claimed that the negative and positive correlations are due to the surface evaporative cooling and temperature advection, respectively.

c. Changes in the precipitation type and intensity

The model precipitation was analyzed by dividing it into convective precipitation (CP) and nonconvective precipitation (NCP) and the type of the precipitation

increase by D_RCPs was examined. Figure 13 describes NCP and CP in D_Historical and their changes for D_RCP8.5. The BCM front is a stationary front occurring when the Okhotsk sea air mass (mP) and the North Pacific air mass (mT) confront each other and basically consists of NCP. On the other hand, strong precipitation related to the local convection is accompanied in the stationary front and D_Historical illustrates this properly (contours in Fig. 13a,b). That is, although NCP is distributed continuously over a wide area, including high latitude regions, CP is stronger than NCP and appears in a narrow area. NCP, which is distributed widely up to the regions south of 42°N before late May, moves northward from the middle of June. CP also moves

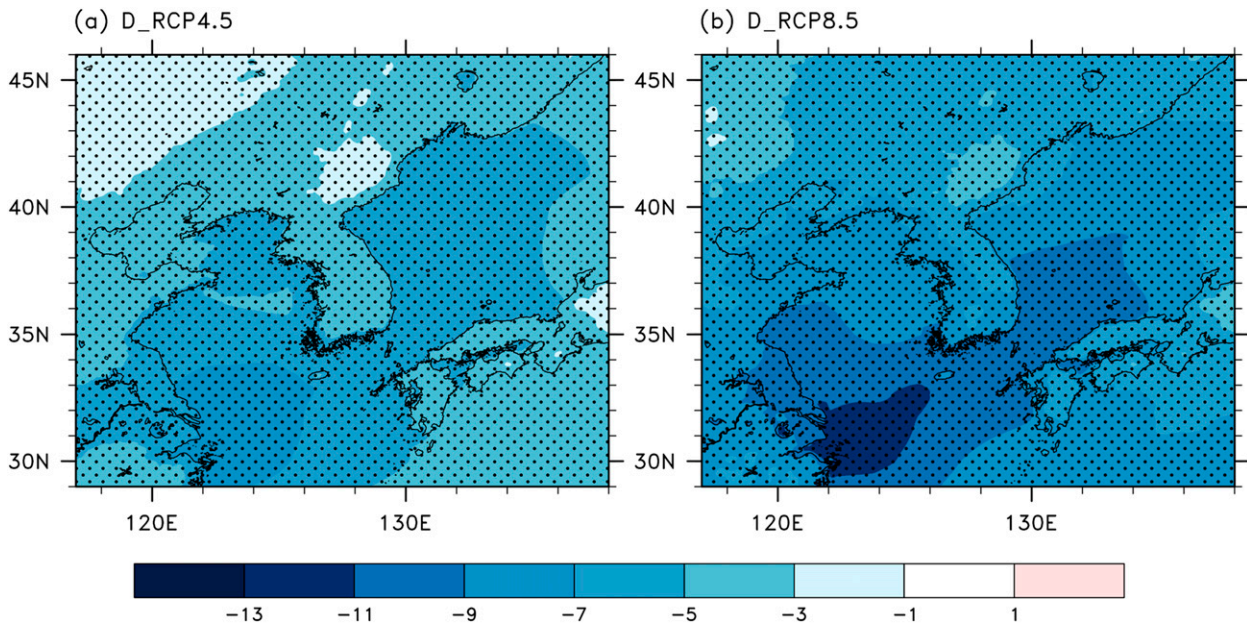


FIG. 14. Changes in the equivalent potential temperature difference ($\Delta\theta_e$; 700 hPa–surface) for (a) D_RCP4.5 and (b) D_RCP8.5. Unit is kelvins. The black dotted stippling indicates statistical significance at the 5% significance level of the t test.

northward accordingly. CP is stronger than NCP and prominent at the southern part of the Korean Peninsula. Therefore, D_Historical simulates the movements of the stationary front and related distribution and characteristics of NCP and CP reasonably well.

In D_RCP8.5, the changes in CP are similar to the increases in total precipitation, as shown in Fig. 8b. This means that precipitation changes in D_RCP8.5 are due mostly to the increase in CP. The changes of CP in D_RCP8.5 from the middle of June to early July are significant at the 5% significance level of the t test. That is, the changes in NCP are relatively small and the decreases are clear in early and mid-July. The increase in total precipitation after late July appear to be related to the enhancement of convective activity because NCP weakly contributes to the increase in precipitation during that period (Fig. 8b). The northward passage of the BCM front is due to the expansion of the North Pacific High over the region. Thus, the increase of CP in late July is related to the convective activities triggered mainly by local effects in the warm and humid maritime air mass occupying the region after the passage of the BCM front.

From the simulation of summertime (72 h from 0000 UTC 11 June 2003) precipitation over the central United States using WRF2.1 at grid spacings of 48, 24, 12, and 6 km with 30 vertical levels, Galewsky (2005) claimed that the probability of CP exceeding 20% of the total precipitation at grid points where the total precipitation exceeds 20 mm is detectable and relatively more independent from the grid spacing for the

Kain–Fritsch scheme than that for the Betts–Miller–Janjic scheme. In general, the resolved (i.e., nonconvective) contribution increases as the resolution becomes finer. In addition, the more active the trigger function in cumulus parameterizations, the greater the parameterized precipitation. Yu et al. (2011) investigated the impacts of various cumulus convective schemes of WRF and produced summer precipitation from 2000 to 2009 over China with 60-km horizontal resolution and 31 sigma levels. They argued that the Kain–Fritsch (Betts–Miller–Janjic) scheme tends to overestimate summer heavy (light) precipitation. This suggests that the total precipitation and ratio of CP to the total can be dependent on the cumulus parameterization schemes and grid spacing.

To understand the changes of CP, the difference in the equivalent potential temperature was calculated and is demonstrated in Fig. 14. The figure shows the moist static stability changes in the lower atmosphere obtained from the differences in equivalent potential temperatures ($\Delta\theta_e$) between 700 hPa and the surface. The spatial correlation coefficients between changes of the moist static stability and CP are -0.87 and -0.87 for D_RCP4.5 and D_RCP8.5, respectively. All differences in $\Delta\theta_e$ between D_RCPs and D_Historical are significant at the 5% significance level of the t test in domain. The $\Delta\theta_e$ differences between the two D_RCPs and D_Historical are all negative in the entire domain, which suggests that the atmospheric condition will become overall moist statically unstable in both scenarios. The difference in D_RCP8.5 is larger than

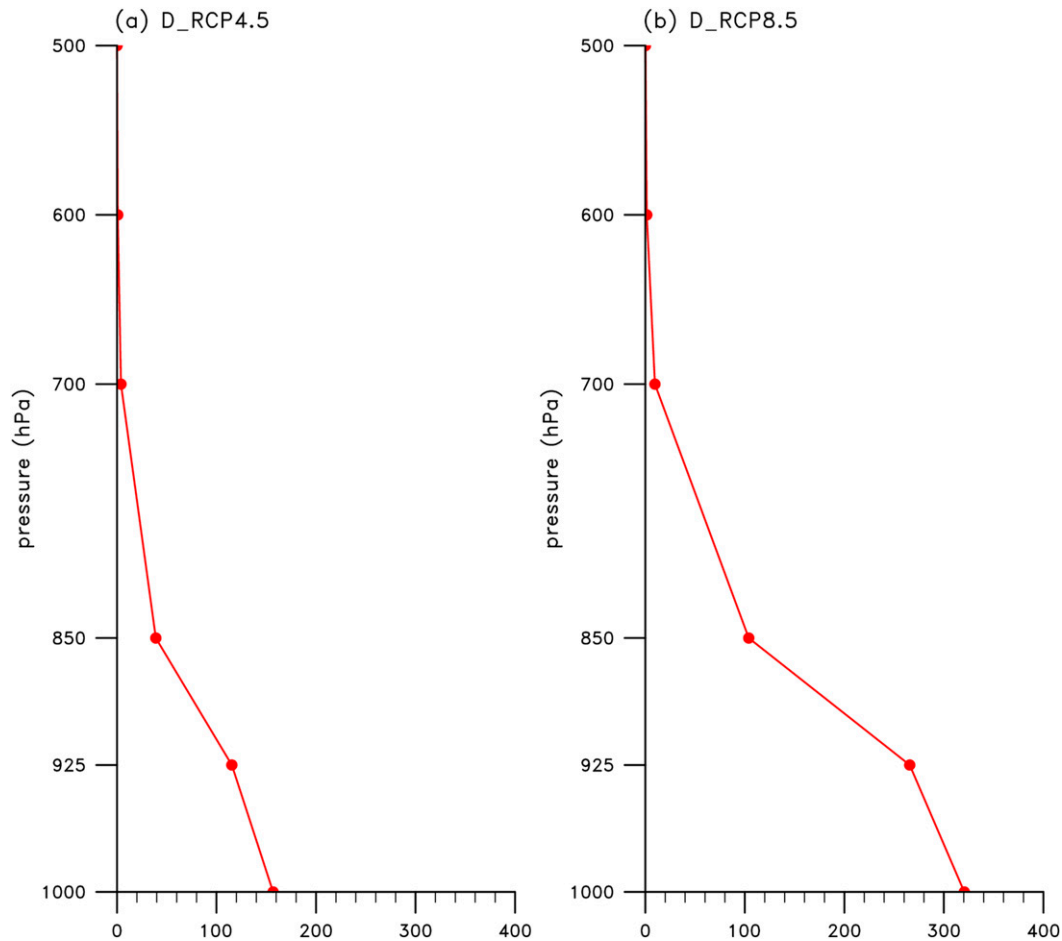


FIG. 15. Changes in CAPE over the south region of the Korean Peninsula and Kyushu in Japan (33° – 36° N, 124° – 132° E) for (a) D_RCP4.5 and (b) D_RCP8.5. Unit is J kg^{-1} . The red dots indicate statistical significance at the 5% level of the t test.

that in D_RCP4.5. Therefore, in D_RCP4.5 and D_RCP8.5, there is less moist static stability in the low-level atmosphere than in D_Historical and this increased instability appears to be related to the increases in CP.

Figure 15 exhibits the vertical profiles of the changes in convective available potential energy (CAPE) averaged for the southern region of the Korean Peninsula and Kyushu in Japan (33° – 36° N, 124° – 132° E), where increases of CP were clearly projected. In the case of D_RCP4.5, the increases of CAPE are clear at levels below 700 hPa (Fig. 15a). In D_RCP8.5, the magnitudes of the changes in CAPE are larger than those in D_RCP4.5 (Fig. 15b). This suggests that the increases of CAPE at low levels appear to contribute to the increase of CP in this region.

To determine the contribution of stratification and water vapor distribution to the reduced moist static stability, the dry and moist static energies for D_RCP8.5 were calculated. The dry static energy is defined as $s \equiv c_p T + gz$, where c_p is the specific heat of dry air at

constant pressure ($=1004 \text{ J K}^{-1} \text{ kg}^{-1}$), T the temperature (K), g the gravitational constant and z the height above the surface. Moist static energy is defined as $h \equiv s + L_c q$, where L_c is the latent heat of condensation at 0°C ($2.5 \times 10^6 \text{ J kg}^{-1}$) and q the water vapor specific humidity. As shown in Fig. 16, the change in moist static energy largely exceeds that of dry static energy, particularly at the low level. This implies that the reduction of moist static stability in the projected climate is mainly due to the increase of moisture at low level in this region.

Figure 17 demonstrates the changes in precipitation intensity during 30 days from the middle of June to the middle of July when the frontal activities are most active in the Korean Peninsula. The precipitation intensity was defined as the upper-5th-percentile daily precipitation divided by the number of its frequency. In the case of D_RCP4.5, the precipitation intensity became stronger (weaker) than D_Historical in the southern region of the Korean Peninsula and the East Sea (the northern region of domain). Overall, the area-averaged intensity of

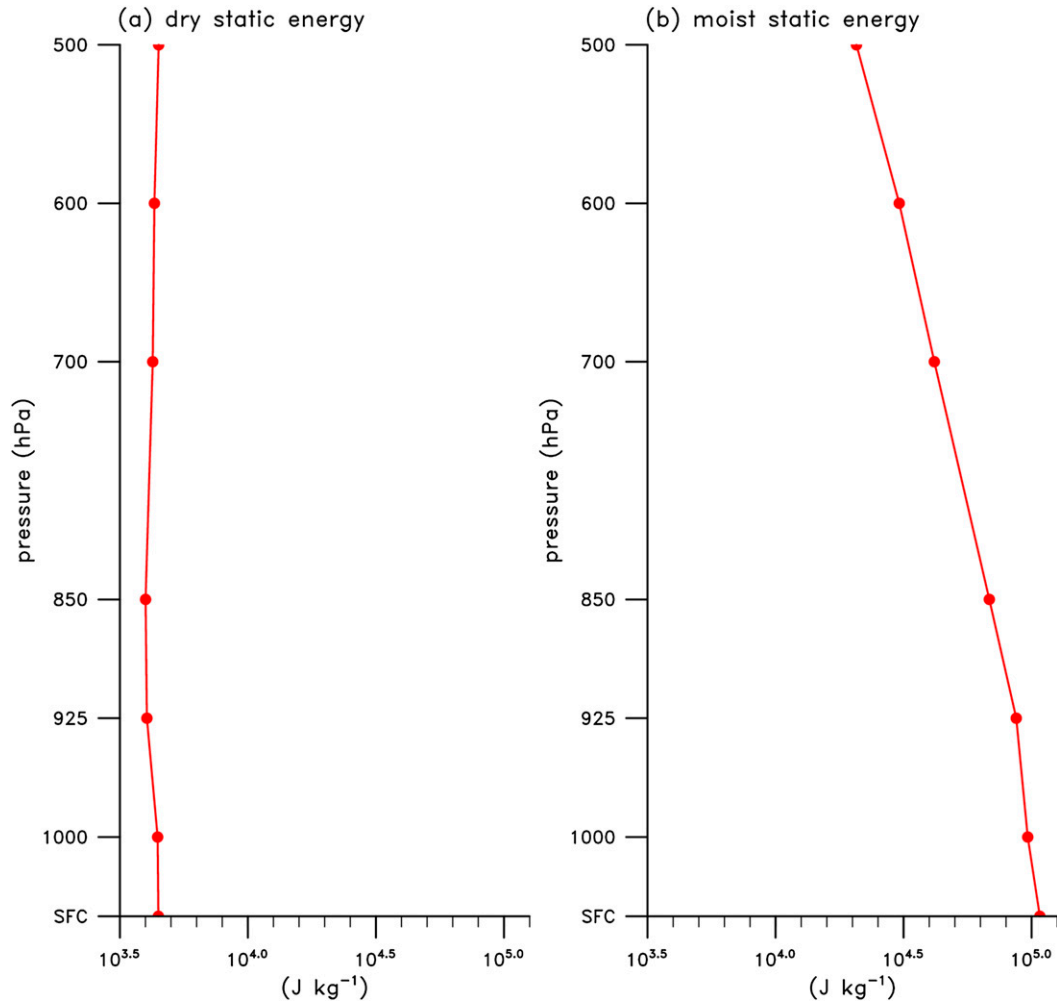


FIG. 16. Changes of (a) dry static energy and (b) moist static energy over the south region of the Korean Peninsula and Kyushu in Japan (33° – 36° N, 124° – 132° E) for D_RCP8.5. Unit is J kg^{-1} . The red dots indicate statistical significance at the 5% level of the t test.

D_RCP4.5 increases by at least 22% compared to that of D_Historical. The precipitation intensity in D_RCP8.5 was 5%–55% more robust than that in D_Historical in most of the domain, except for the northern coastal region of the Korean Peninsula, the Yellow Sea, and the southeastern part of domain. The area-averaged intensity of D_RCP8.5 increases by 38% compared to that in D_Historical.

5. Summary and conclusions

This study analyzed the changes in precipitation related to the BCM front and focused mainly on changma using D_Historical (1981–2010) and D_RCPs (2071–2100) downscaled to a 12.5-km horizontal resolution for the NEA domain. WRF was used for downscaling based on the RCPs produced by HadGEM2-AO.

The general patterns of the MJJ-averaged precipitation in D_Historical were similar to those in TRMM, including terrain-following features. In particular, the precipitation patterns in South Korea were similar to the in situ meteorological observation. The temporal and spatial variations of precipitation associated with the BCM front according to the expansion of the North Pacific high were simulated well compared to TRMM. Although the times of northward movements of the rainband in D_Historical were slightly later than those in TRMM, the speed of northward movements and spatial distribution over time were similar to those in TRMM. In addition, the patterns and evolution of CP and NCP simulated in D_Historical depicted the BCM-related precipitation characteristics. Because the characteristics of the precipitation in this region downscaled by WRF during this period were well simulated, the

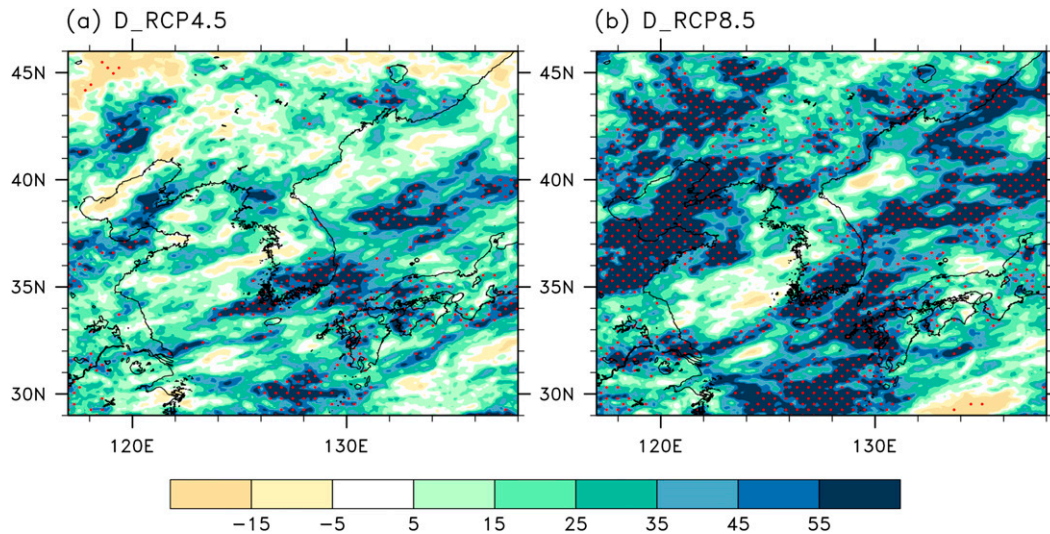


FIG. 17. Changes in 5% extreme precipitation intensity from 15 Jun to 14 Jul for (a) D_RCP4.5 and (b) D_RCP8.5. Units are percentages. The grid points dotted with red indicate statistical significance at the 5% level of the t test.

precipitation changes projected by D_RCPs were considered to be reliable and were analyzed further in detail.

In D_RCPs, changma is expected to develop approximately 10 days earlier and weaken or decay approximately 10 days earlier in the Korean Peninsula than in D_Historical. That is, although the changma duration is expected to be similar to that in D_Historical, the precipitation during the changma period is expected to be higher than that in D_Historical, which means that the precipitation intensity will increase during this period. Increases in precipitation over the Korean Peninsula during the MJJ period were higher in D_RCP8.5 than in D_RCP4.5. These increases were attributed to increases in moist static instability in the lower atmosphere because of decreases in $\Delta\theta_e$. The increases in moist air inflows into this region were attributed to northward moisture transport. Both the increases in 850-hPa moisture flux flowing into the region and in static instability were larger in D_RCP8.5 than in D_RCP4.5. In addition, CP in D_RCPs clearly increased during the changma period, which was attributed to the increase in convective activity because of the increased instability in the lower atmosphere. On the other hand, NCP in D_RCPs was not changed significantly and actually decreased in the late part of the changma period (early and mid-July). The heavy precipitation intensity (upper 5th percentile) in D_RCP4.5 and D_RCP8.5 from the middle of June to the middle of July is expected to increase by at least 22% and 38% compared to that in D_Historical, respectively. These

expected increases in precipitation and its intensity are similar to the results of several studies using regional models based on SRES A2 (Kurihara et al. 2005) and global models based on SRES A2 and B2 (Jiang et al. 2004; Kitoh et al. 2005).

The uncertainty needs to be considered since climate projection is dependent on the models used (global and/or regional), analysis periods and seasons, and target domains (e.g., Gao et al. 2013; Oh et al. 2014). Because this study used a single CMIP5 model and a single regional climate model for projecting BCM-related precipitation, additional studies using more diverse CMIP5 models and regional climate model results may provide more reliable projections.

Acknowledgments. This work was funded by the Korea Meteorological Administration Research and Development Program under Grant CATER 2012-3083 and carried out with the support of the Rural Development Administration Cooperative Research Program for Agriculture Science and Technology Development Project PJ009353. The authors wish to division of supercomputer management of the Korea Meteorological Administration for providing us with the supercomputer resource and consulting on technical support.

REFERENCES

- Ahn, J.-B., J.-H. Ryu, E.-H. Cho, and J.-Y. Park, 1997: A Study of correlations between Air-Temperature and Precipitation of Korean and SST around Korean Peninsula (in Korean with English abstract). *Asia-Pac. J. Atmos. Sci.*, **2**, 327–336.

- , J. Lee, and E.-S. Im, 2012: The reproducibility of surface air temperature over South Korea using dynamical downscaling and statistical correction. *J. Meteor. Soc. Japan*, **90**, 493–507, doi:10.2151/jmsj.2012-404.
- Baek, H.-J., and Coauthors, 2013: Climate change in the 21st century simulated by HadGEM2-AO under representative concentration pathways. *Asia-Pac. J. Atmos. Sci.*, **49**, 603–618, doi:10.1007/s13143-013-0053-7.
- Chen, F., and J. Dudhia, 2001: Coupling an advanced land-surface/hydrology model with the Penn State/NCAR MM5 modeling system. Part I: Model description and implementation. *Mon. Wea. Rev.*, **129**, 569–585, doi:10.1175/1520-0493(2001)129<0569:CAALSH>2.0.CO;2.
- Chen, H., and J. Sun, 2013: Projected change in East Asian summer monsoon precipitation under RCP scenario. *Meteor. Atmos. Phys.*, **121**, 55–77, doi:10.1007/s00703-013-0257-5.
- Collins, W. D., J. K. Hackney, and D. P. Edwards, 2002: An updated parameterization for infrared emission and absorption by water vapor in the National Center for Atmospheric Research Community Atmosphere Model. *J. Geophys. Res.*, **107**, 4664, doi:10.1029/2001JD001365.
- Collins, W. J., and Coauthors, 2011: Development and evaluation of an Earth-system model—HadGEM2. *Geosci. Model Dev. Discuss.*, **4**, 997–1062, doi:10.5194/gmdd-4-997-2011.
- Ding, H., R. J. Greatbatch, W. Park, M. Latif, V. A. Semenov, and X. Sun, 2014: The variability of the East Asian summer monsoon and its relationship to ENSO in a partially coupled climate model. *Climate Dyn.*, **42**, 367–379, doi:10.1007/s00382-012-1642-3.
- Ding, Y., and J. C. L. Chan, 2005: The East Asian summer monsoon: An overview. *Meteor. Atmos. Phys.*, **89**, 117–142, doi:10.1007/s00703-005-0125-z.
- , Z. Wang, and Y. Sun, 2008: Inter-decadal variation of the summer precipitation in East China and its association with decreasing Asian summer monsoon. Part I: Observed evidences. *Int. J. Climatol.*, **28**, 1139–1161, doi:10.1002/joc.1615.
- Galewsky, J., 2005: Quantifying the dependence of convective parameterization activity on horizontal grid spacing in WRF: Preliminary results. WRF-DTC Visitor Program, 8 pp. [Available online at http://www.dtcenter.org/visitors/reports_05/galewsky.pdf.]
- Gao, X.-J., M.-L. Wang, and F. Giorgi, 2013: Climate change over China in the 21st century as simulated by BCC_CSM1.1-RegCM4.0. *Atmos. Oceanic Sci. Lett.*, **6**, 381–386.
- Gastineau, G., H. Le Treut, and L. Li, 2008: Hadley circulation changes under global warming conditions indicated by coupled climate models. *Tellus*, **60A**, 863–884, doi:10.1111/j.1600-0870.2008.00344.x.
- , K. Li, and H. Treut, 2009: The Hadley and Walker circulation changes in global warming conditions described by idealized atmospheric simulations. *J. Climate*, **22**, 3993–4013, doi:10.1175/2009JCLI2794.1.
- Giorgi, F., and C. Shields, 1999: Tests of precipitation parameterizations available in latest version of NCAR regional climate model (RegCM) over continental United States. *J. Geophys. Res.*, **104**, 6353–6375, doi:10.1029/98JD01164.
- Held, I. M., and B. J. Soden, 2006: Robust responses of the hydrological cycle to global warming. *J. Climate*, **19**, 5686–5699, doi:10.1175/JCLI3990.1.
- Hong, S.-Y., J. Dudhia, and S.-H. Chen, 2004: A revised approach to ice microphysical processes for the bulk parameterization of clouds and precipitation. *Mon. Wea. Rev.*, **132**, 103–120, doi:10.1175/1520-0493(2004)132<0103:ARATIM>2.0.CO;2.
- , Y. Noh, and J. Dudhia, 2006: A new vertical diffusion package with an explicit treatment of entrainment processes. *Mon. Wea. Rev.*, **134**, 2318–2341, doi:10.1175/MWR3199.1.
- Hsu, H.-H., T. Zhou, and J. Matsumoto, 2014: East Asian, Indochina and western North Pacific summer monsoon—An update. *Asia-Pac. J. Atmos. Sci.*, **50**, 45–68, doi:10.1007/s13143-014-0027-4.
- Hu, Z.-Z., 1997: Interdecadal variability of summer climate over East Asia and its association with 500-hPa height and global sea surface temperature. *J. Geophys. Res.*, **102**, 19 403–19 412, doi:10.1029/97JD01052.
- , S. Yang, and R. Wu, 2003: Long-term climate variations in China and global warming signals. *J. Geophys. Res.*, **108**, 4614, doi:10.1029/2003JD003651.
- Huffman, G. J., and Coauthors, 2007: The TRMM Multisatellite Precipitation Analysis (TMPA): Quasi-global, multiyear, combined-sensor precipitation estimates at fine scales. *J. Hydrometeorol.*, **8**, 38–55, doi:10.1175/JHM560.1.
- Jiang, D.-B., H.-J. Wang, and X.-M. Lang, 2004: East Asian climate change trend under global warming background. *Chin. J. Geophys.*, **47**, 675–681, doi:10.1002/cjg2.3536.
- Jiménez, P. A., J. Dudhia, J. F. González-Rouco, J. Navarro, J. P. Montávez, and E. García-Bustamante, 2012: A revised scheme for the WRF surface layer formulation. *Mon. Wea. Rev.*, **140**, 898–918, doi:10.1175/MWR-D-11-00056.1.
- Kain, J. S., 2004: The Kain–Fritsch convective parameterization: An update. *J. Appl. Meteor.*, **43**, 170–181, doi:10.1175/1520-0450(2004)043<0170:TKCPAU>2.0.CO;2.
- Kim, K.-Y., and G. North, 1997: EOFs of harmonizable cyclostationary processes. *J. Atmos. Sci.*, **54**, 2416–2427, doi:10.1175/1520-0469(1997)054<2416:EOHCP>2.0.CO;2.
- , and J.-W. Roh, 2010: Physical mechanisms of the wintertime surface air temperature variability in South Korea and the near-7-day oscillations. *J. Climate*, **23**, 2197–2212, doi:10.1175/2009JCLI3348.1.
- Kitoh, A., M. Hosaka, Y. Adachi, and K. Kamiguchi, 2005: Future projections of precipitation characteristics in East Asia simulated by the MRI CGCM2. *Adv. Atmos. Sci.*, **22**, 467–478, doi:10.1007/BF02918481.
- Kripalani, R. H., J. H. Oh, and H. S. Chaudhari, 2007: Response of the East Asian summer monsoon to doubled atmospheric CO₂: Coupled climate models simulations and projections under IPCC AR4. *Theor. Appl. Climatol.*, **87**, 1–28, doi:10.1007/s00704-006-0238-4.
- Kurihara, K., and Coauthors, 2005: Projection of climatic change over Japan due to global warming by high-resolution regional climate model in MRI. *SOLA*, **1**, 97–100, doi:10.2151/sola.2005-026.
- Kusunoki, K., and R. Mizuta, 2008: Future changes in the baiu rain band projected by a 20-km mesh global atmospheric model: Sea surface temperature dependence. *SOLA*, **4**, 85–88, doi:10.2151/sola.2008-022.
- Lee, D. K., and J. G. Park, 2002: A comparison study of moist physics schemes in simulation of East Asian heavy rainfall. *J. Korean Meteor. Soc.*, **38**, 581–592.
- Lee, H.-S., S.-Y. Gan, Y.-H. Byun, H.-S. Kang, Y.-K. Hyun, H.-J. Haek, and W.-T. Kwon, 2009: Evaluation of HadGEM2-AO based on historical simulation of IPCC AR5 (in Korean). *Proc. Conf. on Autumn Meeting of Korean Meteorological Society*, Daegu, South Korea, Korean Meteorological Society, 272–273.
- , —, H.-J. Baek, and C.-H. Cho, 2010: Evaluation of the pre-industrial simulation of HadGEM2-AO. *Proc. Conf. on Autumn Meeting of Korean Meteorological Society*, Busan, South Korea, Korean Meteorological Society, 146–147.

- Lee, S.-S., and K.-H. Seo, 2013: The development of a statistical forecast model for changma. *Wea. Forecasting*, **28**, 1304–1321, doi:10.1175/WAF-D-13-00003.1.
- Levine, X. J., and T. Schneider, 2011: Response of the Hadley circulation to climate change in an aquaplanet GCM coupled to a simple representation of ocean heat transport. *J. Atmos. Sci.*, **68**, 769–783, doi:10.1175/2010JAS3553.1.
- Li, J., Z. Wu, Z. Jiang, and J. He, 2010: Can global warming strengthen the East Asian summer monsoon? *J. Climate*, **23**, 6696–6705, doi:10.1175/2010JCLI3434.1.
- Liu, J., B. Wang, and J. Yang, 2008: Forced and internal modes of variability of the East Asian summer monsoon. *Climate Past*, **4**, 225–233, doi:10.5194/cp-4-225-2008.
- Liu, X., and Y. Wang, 2011: Contrasting impacts of spring thermal conditions over Tibetan Plateau on late-spring to early-summer precipitation in southeast China. *Atmos. Sci. Lett.*, **12**, 309–315, doi:10.1002/asl.343.
- Liu, Y., F. Giorgi, and W. M. Washington, 1994: Simulation of summer monsoon climate over East Asia with an NCAR regional climate model. *Mon. Wea. Rev.*, **122**, 2331–2348, doi:10.1175/1520-0493(1994)122<2331:SOSMCO>2.0.CO;2.
- Meinshausen, M., and Coauthors, 2011: The RCP greenhouse gas concentrations and their extension from 1765 to 2300. *Climatic Change*, **109**, 213–241, doi:10.1007/s10584-011-0156-z.
- Menon, S., J. Hansen, L. Nazarenko, and Y. Luo, 2002: Climate effects of black carbon aerosols in China and India. *Science*, **297**, 2250–2253, doi:10.1126/science.1075159.
- Moteki, O., and A. Manda, 2013: Seasonal migration of the baiu frontal zone over the East China Sea: Sea surface temperature effect. *SOLA*, **9**, 19–22, doi:10.2151/sola.2013-005.
- Oh, J. H., W. T. Kwon, and S. B. Ryoo, 1997: Review of the researches on changma and future observational study (KORMEX). *Adv. Atmos. Sci.*, **14**, 207–220, doi:10.1007/s00376-997-0020-2.
- Oh, S.-G., J.-H. Park, S.-H. Lee, and M.-S. Suh, 2014: Assessment of the RegCM4 over East Asia and future precipitation change adapted to the RCP scenarios. *J. Geophys. Res.*, **119**, 2913–2927, doi:10.1002/2013JD020693.
- Qian, W., and Y. Zhu, 2002: The Comparison between summer monsoon components over East Asia and South Asia. *J. Geosci. China*, **4**, 17–32.
- Qian, Y. F., Y. Q. Zheng, Y. Zhang, and M. Q. Miao, 2003: Responses of China's summer monsoon climate to snow anomaly over the Tibetan Plateau. *Int. J. Climatol.*, **23**, 593–613, doi:10.1002/joc.901.
- Ramanathan, V., and Coauthors, 2005: Atmospheric brown clouds: Impacts on South Asian climate and hydrological cycle. *Proc. Natl. Acad. Sci. USA*, **102**, 5326–5333, doi:10.1073/pnas.0500656102.
- Sénési, S., P. Bougeault, J.-L. Chêze, P. Cosentino, and R.-M. Thepenier, 1996: The Vason-La-Pomaine flash flood: Mesoscale analysis and predictability issues. *Wea. Forecasting*, **11**, 417–442, doi:10.1175/1520-0434(1996)011<0417:TVALRFF>2.0.CO;2.
- Sun, Y., and Y. Ding, 2010: A projection of future changes in summer precipitation and monsoon in East Asia. *Sci. China*, **53D**, 284–300, doi:10.1007/s11430-009-0123-y.
- Tanaka, H. L., N. Ishizaki, and D. Nohara, 2005: Intercomparison of the intensities and trends of Hadley, Walker and monsoon circulations in the global warming predictions. *SOLA*, **1**, 77–80, doi:10.2151/sola.2005-021.
- Tao, S.-Y., and L.-X. Chen, 1987: A review of recent research on the East Asian summer monsoon in China. *Monsoon Meteorology*, C.-P. Chang and T. N. Krishnamurti, Eds., Oxford University Press, 60–92.
- Ueda, H., A. Iwai, K. Kuwako, and M. E. Hori, 2006: Impact of anthropogenic forcing on the Asian summer monsoon simulated by 8 GCMs. *Geophys. Res. Lett.*, **33**, L06703, doi:10.1029/2005GL025336.
- Vecchi, G. A., and B. J. Soden, 2007: Global warming and the weakening of the tropical circulation. *J. Climate*, **20**, 4316–4340, doi:10.1175/JCLI4258.1.
- Wang, B., Z. Wu, J. Li, J. Liu, C.-P. Chang, Y. Ding, and G. Wu, 2008: How to measure the strength of the East Asian summer monsoon. *J. Climate*, **21**, 4449–4463, doi:10.1175/2008JCLI2183.1.
- Wang, H., 2001: The weakening of the Asian monsoon circulation after the end of 1970's. *Adv. Atmos. Sci.*, **18**, 376–386, doi:10.1007/BF02919316.
- , 2002: The instability of the East Asian summer monsoon-ENSO relations. *Adv. Atmos. Sci.*, **19**, 1–11, doi:10.1007/s00376-002-0029-5.
- , and H. Chen, 2012: Climate control for southeastern China moisture and precipitation: Indian or East Asian monsoon? *J. Geophys. Res.*, **117**, D12109, doi:10.1029/2012JD017734.
- , and Coauthors, 2012: Extreme climate in China: Facts, simulation and projection. *Meteor. Z.*, **21**, 279–304, doi:10.1127/0941-2948/2012/0330.
- Wu, R., and B. Wang, 2002: A contrast of the East Asian summer monsoon-ENSO relationship between 1962–77 and 1978–93. *J. Climate*, **15**, 3266–3279, doi:10.1175/1520-0442(2002)015<3266:ACOTEA>2.0.CO;2.
- Wu, Z., J. Li, J. He, and Z. Jiang, 2006: Occurrence of droughts and floods during the normal summer monsoons in the mid- and lower reaches of the Yangtze River. *Geophys. Res. Lett.*, **33**, L05813, doi:10.1029/2005GL024487.
- Xu, Q., 2001: Abrupt change of the mid-summer climate in central East China by the influence of atmospheric pollution. *Atmos. Environ.*, **35**, 5029–5040, doi:10.1016/S1352-2310(01)00315-6.
- Yu, E., H. Wang, Y. Gao, and J. Sun, 2011: Impacts of cumulus convective parameterization schemes on summer monsoon precipitation simulation over China. *Acta Meteor. Sin.*, **25**, 581–592, doi:10.1007/s13351-011-0504-y.
- Yu, R., and T. Zhou, 2007: Seasonality and three-dimensional structure of the interdecadal change in East Asian monsoon. *J. Climate*, **20**, 5344–5355, doi:10.1175/2007JCLI1559.1.
- , B. Wang, and T. Zhou, 2004: Tropospheric cooling and summer monsoon weakening trend over East Asia. *Geophys. Res. Lett.*, **31**, L22212, doi:10.1029/2004GL021270.
- Zheng, Y., Q. Xu, and D. J. Stensrud, 1995: A numerical simulation of the 7 May 1985 mesoscale convective system. *Mon. Wea. Rev.*, **123**, 1781–1799, doi:10.1175/1520-0493(1995)123<1781:ANSOTM>2.0.CO;2.
- Zhou, T., D. Gong, J. Li, and B. Li, 2009: Detecting and understanding the multi-decadal variability of the East Asian summer monsoon—Recent progress and state of affairs. *Meteor. Z.*, **18**, 455–467, doi:10.1127/0941-2948/2009/0396.
- Zhu, C., B. Wang, W. Qian, and B. Zhang, 2012: Recent weakening of northern East Asian summer monsoon: A possible response to global warming. *Geophys. Res. Lett.*, **39**, L09701, doi:10.1029/2012GL051155.